1415 N CHERRY AVE
CHICAGO, IL 60642
(312) 281-6900
DMDII.ORG
DMDII@UILABS.ORG

DMDII
a UI LABS Collaboration
DIGITIZING AMERICAN MANUFACTURING

DMDII FINAL PROJECT REPORT

Intelligent Welding: Real Time Monitoring, Diagnosis, Decision and Control using Multi-sensor and Machine Learning

Principle Investigator / Email Address	Didem Ozevin / dozevin@uic.edu
Project Team Lead	University of Illinois at Chicago
Project Designation	University of Illinois at Chicago
UI LABS Contract Number	0220160026
Project Participants	Illinois Tool Works (ITW) and Industrial Measurement Systems (IMS)
DMDII Funding Value	$501,554
Project Team Cost Share	$510,292
Award Date	December 5, 2016
Completion Date	December 31, 2018

SPONSORSHIP DISCLAIMER STATEMENT: This project was completed under the Cooperative Agreement W31P4Q-14-2-0001, between U.S. Army - Army Contracting Command - Redstone and UI LABS on behalf of the Digital Manufacturing and Design Innovation Institute. Any opinions, findings, and conclusions or recommendations expressed in this material are those of the author(s) and do not necessarily reflect the views of the Department of the Army.

TABLE OF CONTENTS

I. EXECUTIVE SUMMARY

In this project, the industry problem of real-time weld quality assurance is studied. An automated weld quality assurance can increase the efficiency and the productivity of weld manufacturing. In order to ensure an adequate weld quality, the selection of proper evaluation approaches is critical. Currently, inspections are usually conducted either destructively or in the post-weld stage. Thus, if defects are found in welded product, few of them can be remedied. This may result in the disposal of expensive material, thus decreasing overall productivity. Therefore, an efficient nondestructive weld quality monitoring method is critically needed.

The problem is tackled by integrating multiple sensor outputs into a machine learning algorithm. With proper real-time weld monitoring methods, weld defects are expected to be recognized, and the welder can correct the weld parameter immediately. Whether in a manual or an automated weld process, the experience of the welder is a decisive factor. In addition, it is difficult for the welder to make a rapid and appropriate decision with a high number of parameters from the welding machine and monitoring system. Meanwhile, with a manual decision involved, the automaticity of the weld is limited. With the aim to solve this problem, intelligent decisions in response to process and monitoring variables offer a great potential solution. Through building a training set, machine learning algorithms can analyze the data—including weld parameters and monitoring variables during the weld process—assess the weld quality, and give a reasonable assessment. By keeping collected data and improving the training set during the weld, the accuracy of the machine learning algorithm can subsequently be improved over time. The sensor data utilized in the machine learning algorithm include acoustic emission (hit driven and time driven) and welding data (gas flow rate, current and voltage inputs). The acoustic emission (AE) associated with weld parameter monitoring is chosen as the real-time monitoring methods for automated welding. That is because a variety of acoustic activities are generated within the welding process. The algorithm is evaluated using data recorded at three laboratories in UIC, ITW Miller, and John Deere. Multiple machine learning algorithms are tested. Additionally, a new miniaturized micro-electro-mechanical systems (MEMS) based device is manufactured for the development of low-cost welding monitoring technology. Thus, an automated defect monitoring system can be achieved by utilizing machine learning methods, which would save time from post-weld inspection. On the other hand, it can reduce dependence on human experts, or assist human monitors to notice missed detection.

The main project outcomes and recommendations are as follows:

- It is determined that Gas Tungsten Arc Welding (GTAW) is an acoustically quiet manufacturing process as compared to Gas Metal Arc Welding (GMAW). Therefore, the general prediction accuracies are lower.
- The selected machine learning algorithm, Adversarial Sequence Tagging (AST), is successfully applied to GMAW data with the prediction accuracies ranging from 93.6% to 100% using the 52 samples manufactured at John Deere except for two cases.
- While a total of 119 samples were prepared using GTAW and GMAW, it is found that more datasets that include all the variables in weld manufacturing and defects are needed to better train the machine learning algorithm, ultimately resulting in improved performance accuracies.
- It is identified that air-borne ultrasonic is negatively influenced by electromagnetic field induced at the welding torch. Additionally, air-borne sensors are sensitive to slight changes in angles. Therefore, air-borne UT method is implemented in post-weld in situ to assess the weld penetration and heterogeneities, and the measurements are validated with numerical models.
- A MEMS device is designed and characterized. It accommodates two AE sensors and an array of UT sensors on 4 mm x 4 mm space. The advantage of MEMS device is low cost and small footprint that can

be attached to welding torch. While all the sensors are functional, the device requires robust packaging for harsh environmental condition of weld manufacturing.

II. PROJECT REVIEW

a. Project Scope and Objectives: The project scope includes the development of a real time monitoring approach of weld manufacturing to have real time decision making such that errors in welding parameters can be detected and corrected early without ruining the entire weld piece or structure. Two welding methods are investigated: Gas Tungsten Arc Welding (GTAW) and Gas Metal Arc Welding (GMAW). The target industry selected is heavy industry (e.g., Caterpillar, John Deere). The ultimate objective is to make the decision-making automated with machine learning algorithms. The primary defects studied are excessive weld penetration, burn-through and porosity. Initially, acoustic emission, ultrasonics and thermal data were planned to be used in the machine learning algorithms. Due to significant influence of electromagnetic field induced by welding torch, air-borne UT could not be used in real time. Additionally, the complex movement of robotic welding systems makes UT not practical, as the UT transducers should be tuned to a precise angle with respect to surface. The surface emissivity influenced the thermal measurement. Therefore, acoustic emission features together with welding parameters are used for the development of machine learning algorithm. UT is implemented as post-weld and in-situ assessment of weld penetration quantitatively.

b. Technical Approach and Planned Benefits: The technical approach is data-driven algorithm development. For this purpose, 39 GTAW samples were fabricated at UIC, 28 GTAW and GMAW samples were fabricated at ITW Miller, and 52 GMAW samples were fabricated at John Deere laboratories. Acoustic emission and welding sensors were utilized to build the machine learning algorithm for GTAW and GMAW. The welded part consists of a complex microstructure and it may contain weld discontinuity. Welding defects have negative influence on the structural integrity and can potentially damage irreparable final high-cost pieces. In most cases, the weld quality highly depends on the experience of welder. The post-weld inspections are needed to ensure weld quality. The automated weld quality assurance can improve efficiency and productivity. The weld fabrication associated with a real-time monitoring system shows a great potential to substitute manual welding by detecting defects during processing and taking corrective measures undertaken immediately. As all the sensors utilized in this project are non-contact, this is a completely non-intrusive nondestructive evaluation approach. For quantitative assessment of weld penetration using ultrasonics, numerical models are built to further add model-driven data into the assessment. The major planned benefit of *in-situ* UT is to assess the weld condition without disassembling welding parts. The project tasks, the work done and their contribution to the overall project are as follows.

Task 1. Data Analytics for Weld Defects

The milestone of this task was well-separated defect classification using supervised machine learning. As results of this task detailed below, the most effective feature sets to separate the classes of good weld, excessive penetration, burn-through and porosity for GTAW and GMAW are determined. Good weld is defined as the weld penetration without leading to thickness change or hole. Burn-through is defined as an undesirable open hole when the base metal complete. Excessive penetration is defined as the presence of weld metal penetrated all the way the plate thickness without hole. Porosity is defined as the inclusion of air particles inside the weld bead.

Task 1.1 Experimental Design: In this task, the weld variables to produce different weld penetration levels, burn-through and porosity were identified. The material used in this study was A36 low carbon steel with a composition (in weight percent) of 0.07 C, 0.36 Mn, 0.006 P, 0.003 S, and 0.02 Si. The coupons were cut into plates of the following dimensions: 31 × 15 × 0.48 cm^3 (length × width ×

thickness). Weld burn-through is defined as an undesirable defect that occurs as a result of complete melting of the bottom of the plate and formation of an open hole. The excessive heat input for the mass/thickness of the plate being welded is the reason of burn-through. The welding heat input can be calculated using the following equation:

$$Heat\ input\ (kJ/mm) = \frac{Voltage(V) \times Amperage(A) \times 60}{Travel\ speed(mm/s) \times 1000}$$

Our focus in this project is to establish the progression of the weld metal penetration to the onset of burn-through. In other words, there is evidence of partial melting on the back of the work piece (base plate). Complete burn-through occurs when there is a through-hole in the base plate after welding. Bead-on-plate welds were fabricated by increasing the heat input producing different weld penetrations that ultimately ended in a complete burn-through. The heat input was varied by controlling the welding current at constant weld travel speed, or by varying the travel speed while the current and voltage were maintained constant. The welds were assessed visually and microscopically to see the degree of weld penetration and burn-through, and classified according to the degree of burn-through. The weld classification is depicted in Figure 1. The weld coupons are arranged in terms of their weld appearance, acceptability, and the heat input used during their fabrication and presented in Figure 1.

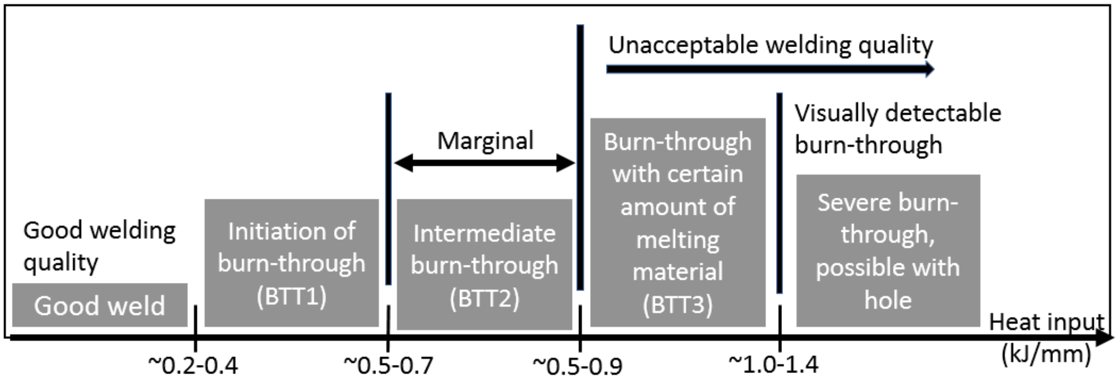

Figure 1 Weld classification based on metallographic analysis and heat input.

The weld penetration increases with heat input as seen in the weld cross section micrographs in Figure 2, but also the weld size (width) increases looking at the top of the weld coupons.

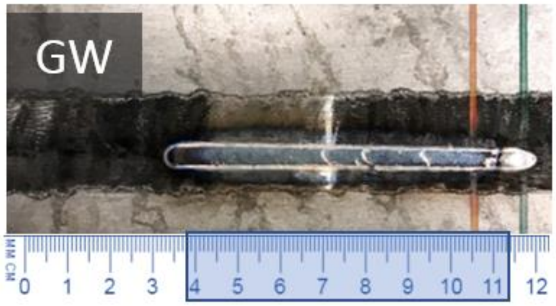

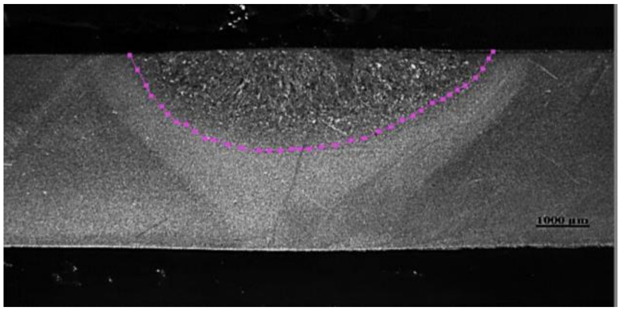

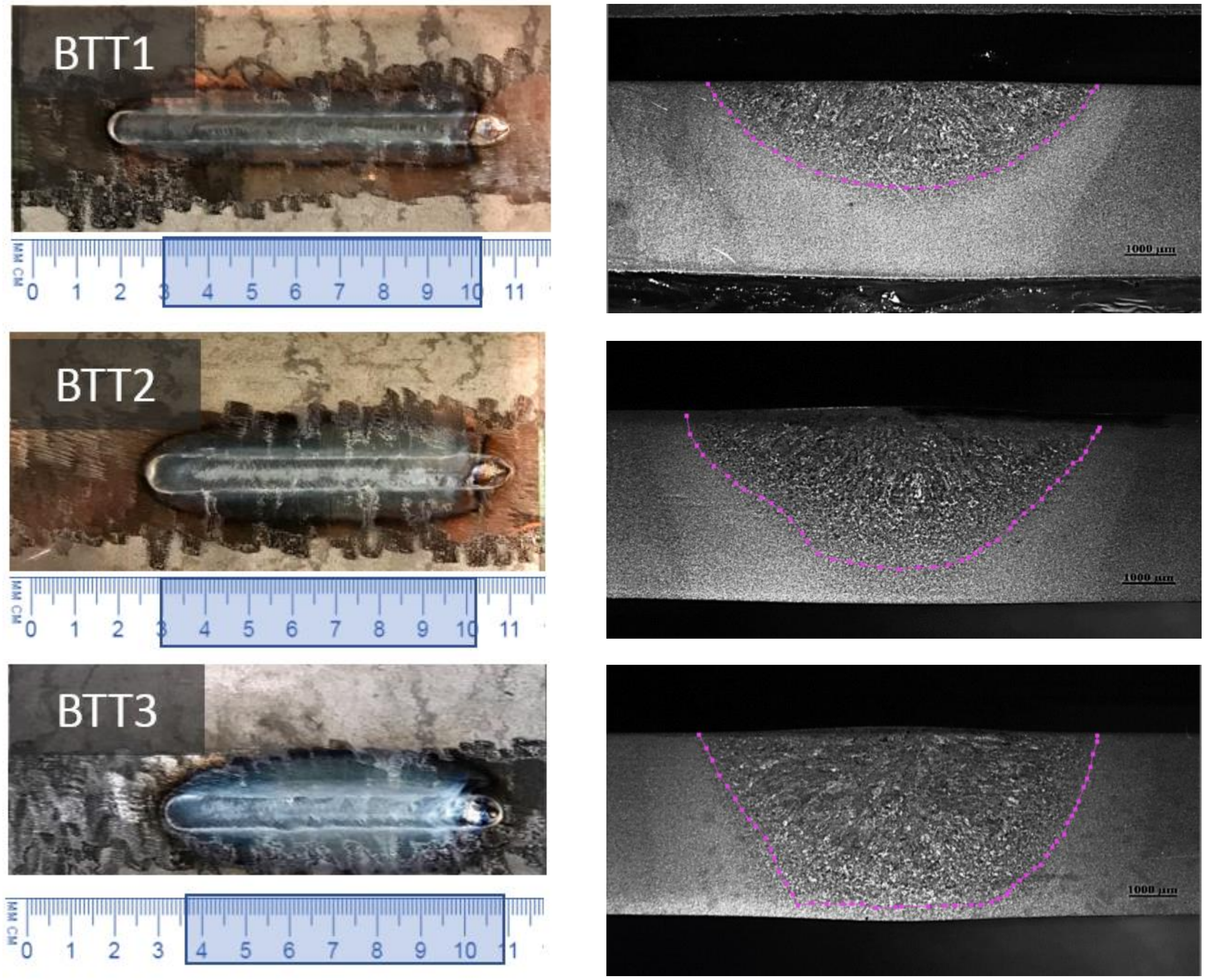

(a) (b)

Figure 2 (a) Top view of welded plates, (b) weld cross sections showing changes in weld penetration with heat input and the onset of burn-through.

For GTAW samples produced at UIC and Miller, porosity inclusions were introduced by varying heat input and mixing Oxygen with Argon in shielding gas as shown in Figure 3. At GMAW samples produced at John Deere, gas flow rate was controlled to introduce porosity, see in Figure 4. Larger porosities were produced at the John Deere samples as compared to the UIC and Miller samples.

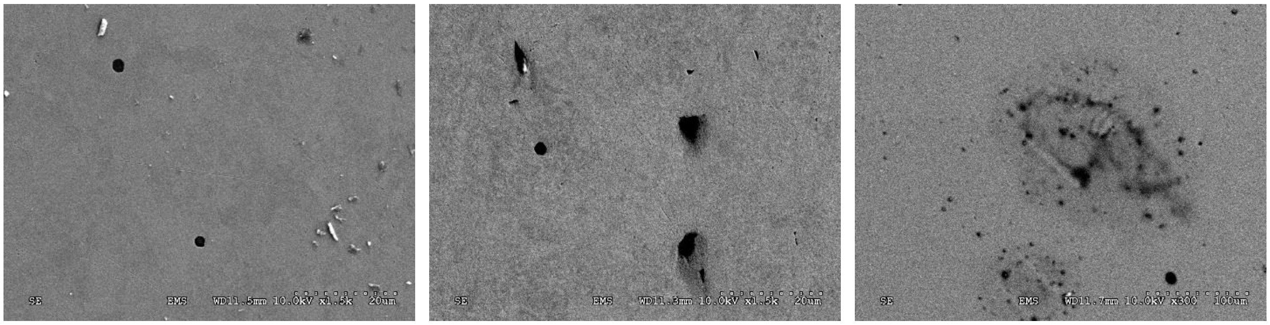

(a) (b) (c)

Figure 3 SEM images indicating porosity in three samples (a) Argon(62.5%) + Argon mixed with 2% O_2 (37.5%), (b) Argon(37.5%) + Argon mixed with 2% O_2 (62.5%), and (c) Argon(25%) + Argon mixed with 2% O_2 (75.0%). The magnifier of (a) and (b) is 20 µm, and the magnifier of (c) is 100 µm.

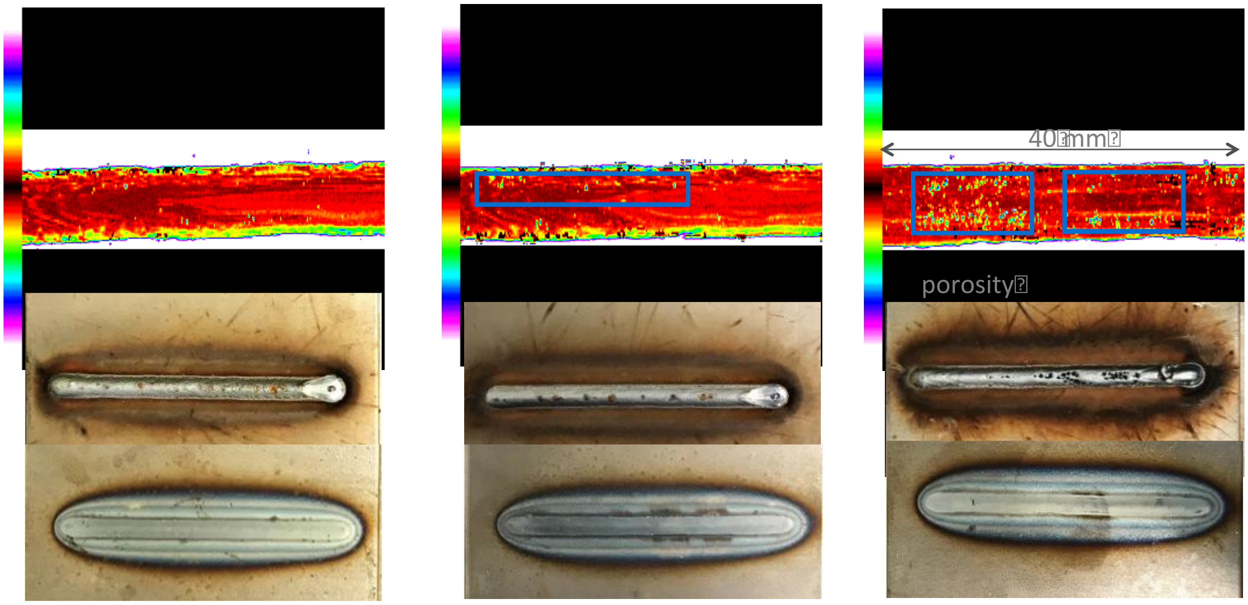

(a) (b) (c)

Figure 4 The acoustic microscope results, (a) JD-P1-TS-1 (no porosity), (b) JD-P1-PO1-3 (low percentage of porosity), and (c) JD-P1-PO3-3 (high percentage of porosity).

Task 1.2 Data Collection with NDE Sensors: Three data sets were collected. This task produced data for understanding the most sensitive features extracted from sensors to weld defects, and using the selected features in machine learning algorithms. The summary of data sets is as follows. The detailed descriptions of data sets can be found in Appendix.

- ***Data Set 1:*** UIC Laboratory, GTAW – good weld, different weld penetrations, burn-through, porosity, total number of samples: 32 samples /39 data sets
- ***Data Set 2:*** Miller Laboratory, GMAW and GTAW, total number of samples: 14 samples / 28 data sets – collected in May 2018.
- ***Data Set 3:*** John Deere Laboratory, GMAW - good weld, different weld penetrations, burn-through, porosity, total number of samples: 48 samples / 52 data sets – collected in October 2018.

For the UT data generation, Figure 5 shows the schematic of experimental and numerical models to build correlation between weld penetration and UT characteristics. The samples produced from data sets 1 and 3 were utilized to build the correlation for GTAW and GMAW, respectively.

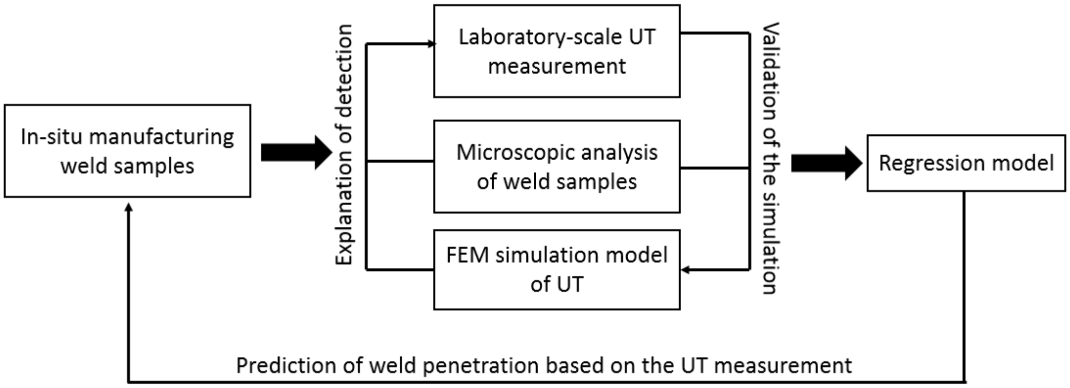

Figure 5 The schematic of experimental and numerical data generation and validation for the weld penetration prediction using UT.

Task 1.3 Correlation of Weld Defects and Input Data: Before applying the machine learning algorithm, AE and UT features relevant to weld defects were identified. Figure 6 shows the cross sectional images of GMAW and GTAW. Both processes produce different weld morphologies (affecting UT measurement) as well as process noise (affecting AE measurement). Therefore, AE and UT characteristics of two welding processes were first defined by visual correlation with the weld defects. Then, they are combined with weld inputs in machine learning algorithms.

- Weld bead accumulated at the top surface and non-uniform weld penetration shape;
- Lots of AE burst signals due to spatters

- Flat top surface and uniform weld penetration shape;
- Very quite process in terms of AE activities

Figure 6 Difference in weld morphologies and process noise for GMAW and GTAW.

AE Features for GTAW: There are two modes to record AE data: the first one is known as hit driven data (HDD) which is based on recording AE signals and features once the signal level detected by AE sensor is above the prescribed threshold; the second mode is the time driven data (TDD) based on recording AE features at each pre-set time interval. Since the TDD data is independent from the threshold, the signals collected during welding are particular to welding process and parameters used. Such data provide an overall correlation between weld quality and AE. The AE data obtained during the welding process contain two main sources: ambient noise (e.g. machinery vibration, and electromagnetic field noise) and welding induced acoustic signals (e.g. metal droplet transfer, flow of the molten pool, phase change due to solidification and solid state phase transformation, liberation of internal tension, dilatations and plastic deformation, crack). Under the same experimental conditions and laboratory environment, ambient noise can be considered constant. The variations in AE data can be linked with the welding induced acoustic signals and the process changes. In this study, the scanner was used to ensure the AE sensors were synchronized with the torch, and the distance between the AE sensors and the welding point was constant. Figure 7 shows ASL (average signal level) and AE absolute energy (calculated by integrating transient signal over 20 ms time window) histories obtained from a good weld (GW) and recorded by two AE sensors. Since R6 sensor exhibits higher sensitivity than WD sensor (40 dB versus 25 dB), the data obtained from R6 are analyzed further.

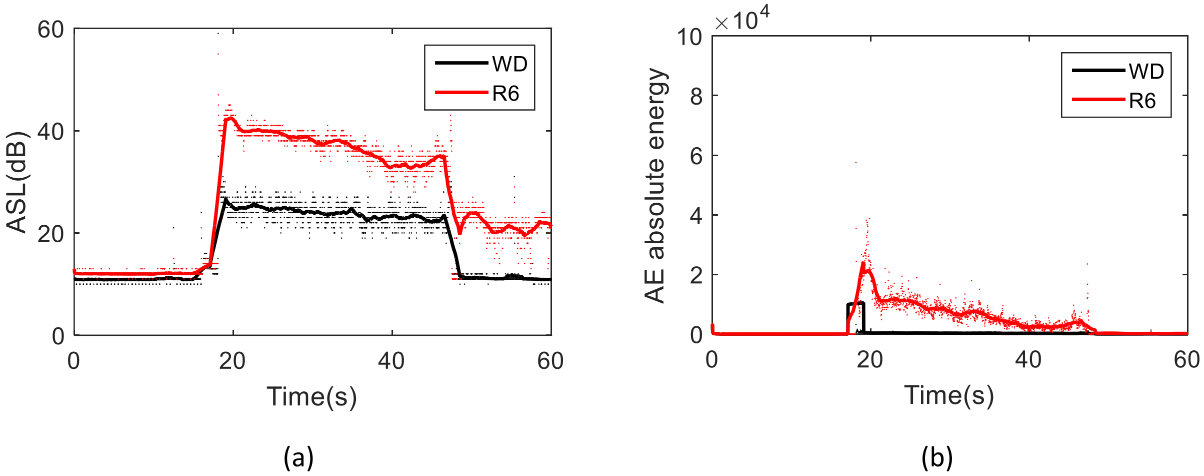

Figure 7 Examples of AE TDD data recorded by two AE sensors from good weld, (a) ASL and (b) AE absolute energy.

Figure 8 shows the AE TDD data corresponding to each of the weld fabricated using different heat inputs, and having different weld penetrations. Though fluctuations are observed in both the average signal level and AE absolute energy, the differences in the welding parameters can be also distinguished by AE. These curves compared with the plots of the calculated heat input show similar correlation. Figure 9 shows the heat input and the AE absolute energy, which indicates that higher acoustical energy corresponds to higher heat input or higher weld penetration. The average values of heat input and AE absolute energy were calculated and marked as blue square on the figure. These two variables can be used to categorize the different welding morphology and quality. However, the difference between GW and BTT1 is implicit due to the similar morphology of welding pool.

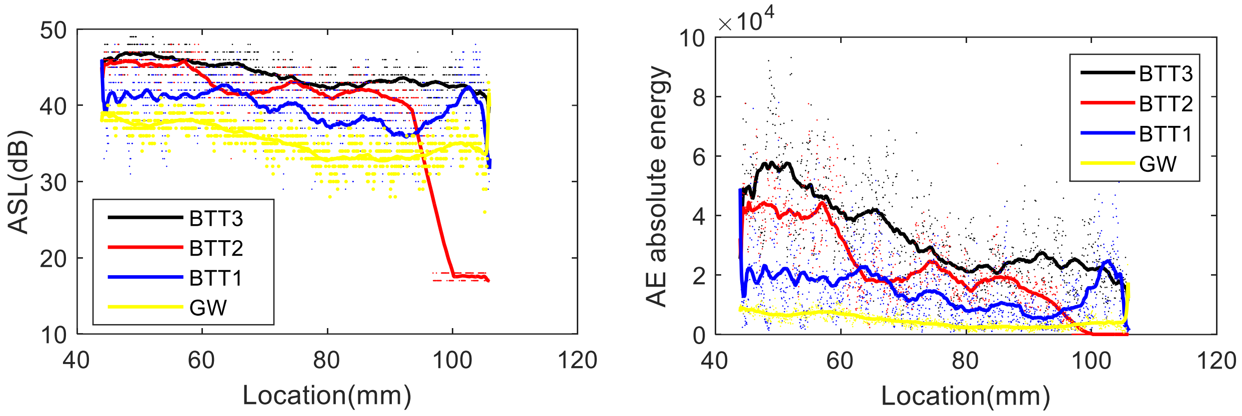

(a) (b)

Figure 8 The correlation of weld classification and AE TDD (a) ASL and (b) absolute energy.

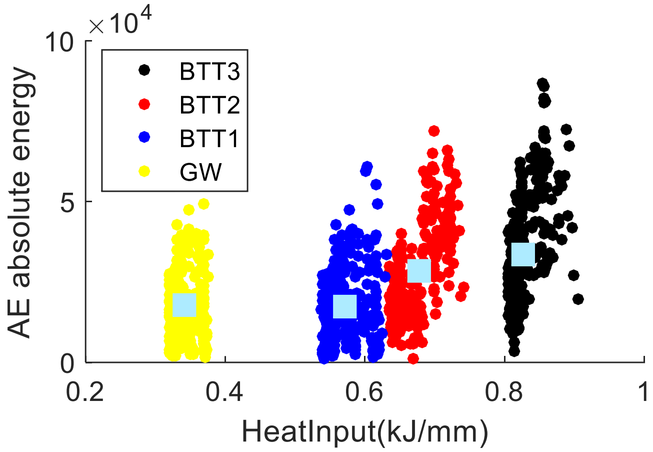

Figure 9 The cross-relationship of heat input and AE absolute energy.

The data collected by the AE sensors also provided information on possible superficial discontinuities or defects in the weld metal. Figure 10(a) shows a superficial indentation or defect, both the ASL scan as well as the AE absolute energy plot showed the exact location of this surface discontinuity at about 85 mm from the start of the weld. The exact location of the superficial was determined by the sudden signal burst that occurred in both cases. This non-uniform welding or weld defect appears to cause a sudden surge in the AE absolute energy.

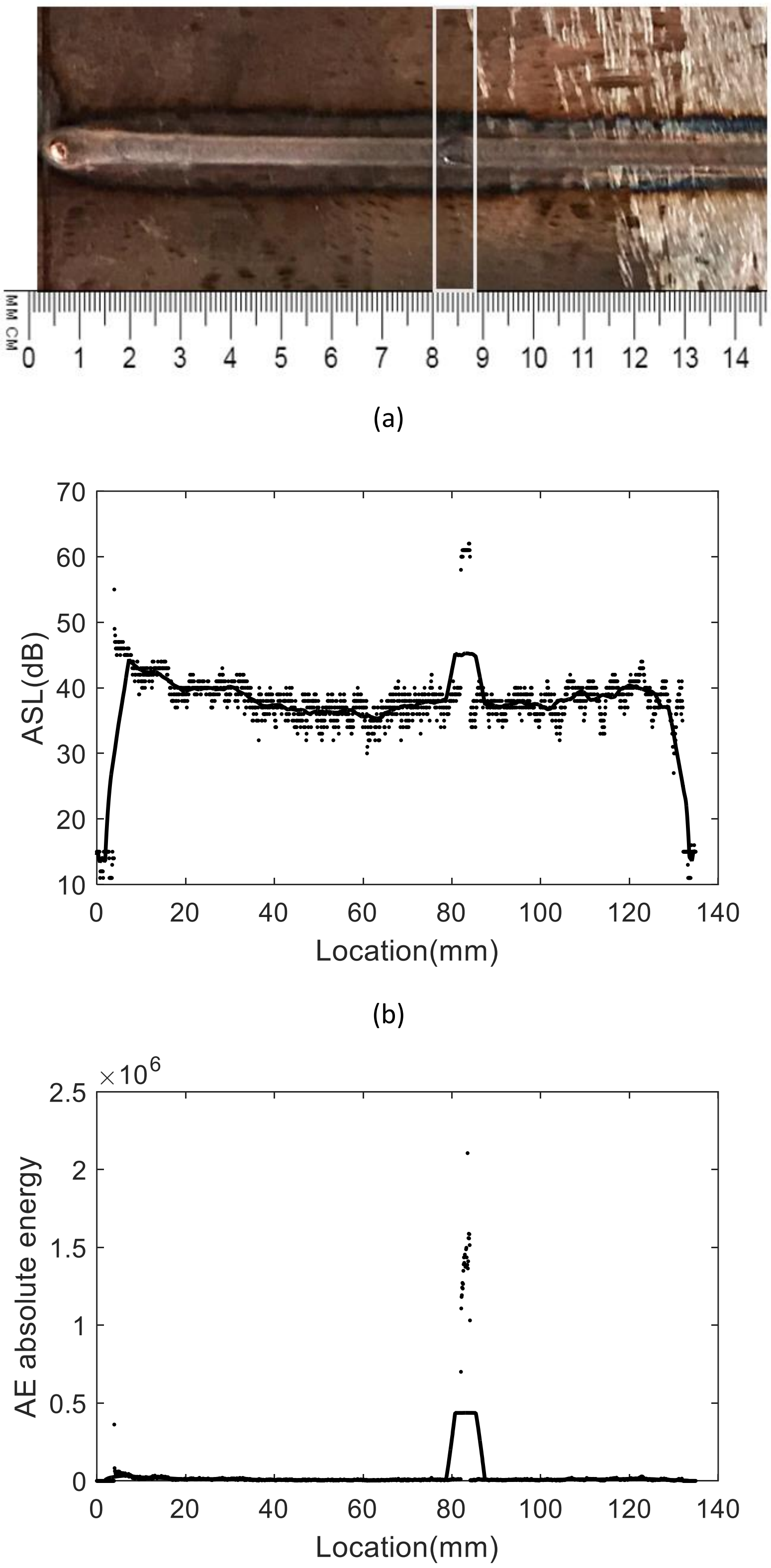

(a)

(b)

(c)

Figure 10 The influence of local weld discontinuity on AE data, (a) the welded plate with discontinuity, (b) ASL and (c) AE absolute energy.

UT Features for GTAW: Ultrasonic inspection has high resolution for detecting defects in weld; however, the challenge with this method is to use a suitable coupling medium to transfer the ultrasonic wave energy into the material. The coupling media commonly used include water, oil, and ultrasonic gel. There are instances, however, where a coupling liquid cannot be used as in the case of in-situ weld inspection where surface temperature and overall contamination risk can be relatively high. The risk can be eliminated by implementing noncontact, air-coupled ultrasonic transducers; however, the main limitations of air-coupled sensing are attenuation in air and acoustic impedance mismatch at the air/steel interface. These limitations have been addressed by recent developments in the design of a newer generation of air-coupled transducers, along with research progress in the field of noncontact ultrasonics. The Lamb-wave-based approach for airborne ultrasonic testing has been implemented using air-couple UT transducers. The A_0 mode is the most detectable Lamb mode in airborne ultrasonic testing due to dominant out-of-plane displacement at the air/solid interface. Therefore, the first step in the generation of Lamb waves using air-coupled transducers is to identify the angle required to create a pure Lamb wave mode. Snell's law suggests that by controlling the angle of the incident wave, different Lamb wave modes can be generated. The phase velocity of the Lamb wave mode is related to the incident angle using the following equation:

$$\theta = \sin^{-1}\frac{c}{c_p}$$

where θ is the angle at which the wave is generated or received, c is the speed of sound in the coupling medium (air in this study), and c_p is the phase velocity of the generated Lamb wave mode in steel. Dispersion curves can be used to calculate the phase velocity related to a Lamb wave mode. The dispersion curve describes the relationship between wave velocity and frequency–thickness content for the solid medium. Figure 11 presents the dispersion curve of the steel plate with the properties listed in Table 1.

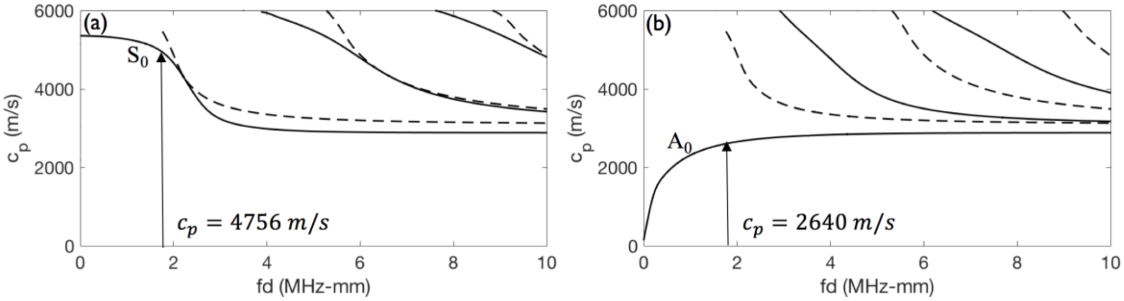

Figure 11 Dispersion curve corresponding to steel plate for (**a**) symmetric modes and (**b**) antisymmetric modes.

Table 1. The material constants of structural steel.

Property	Values		
Density (kg/m^3)	7850		
Young's modulus (MPa)	200 × $\mathbf{10^3}$		
Poisson's ratio	0.33		
Lame constants (MPa)	λ = 150 × $\mathbf{10^3}$		μ = 75 × $\mathbf{10^3}$
Murnaghan constants (MPa)	l = −300 × $\mathbf{10^3}$	m = −620 × $\mathbf{10^3}$	n = −720 × $\mathbf{10^3}$

The thickness of the steel plate is 4.8 mm, and the central frequency of the ultrasonic transducer is 0.4 MHz, which together result in the frequency–thickness (fd) value of 1.96 MHz-mm. As shown in Figure 11, only the fundamental S_0 and A_0 modes exist at this value. The phase velocities for the S_0 and A_0 fundamental modes are calculated as 4,756 and 2,640 m/s, respectively. By using the air velocity of 340 m/s and Equation 2, the angles required to generate the dominant S_0 and A_0 modes are calculated as 4° and 7°, respectively.

Figure 12 demonstrates the experimental setup used to investigate weld defects with the air-coupled ultrasonic method. The measurement system consists of two air-coupled ultrasonic transducers manufactured by Ultran Group with an active area diameter of 19 mm, center frequency of 0.4 MHz, and frequency bandwidth of ±0.117 MHz (down to −6 dB). The transducers are fixed at the required angle of 7° to get the dominant A_0 Lamb wave mode as calculated in the previous section. As observed in Figure 11, a slight change in the transducer angle influences the ultrasonic signal. Therefore, the scanner is designed to keep the angles of the transmitting and receiving transducers consistent throughout the experiments. The distance (S) between the transducers is fixed at 60 mm to allow for a thorough inspection of the welded sample with minimum boundary reflections.

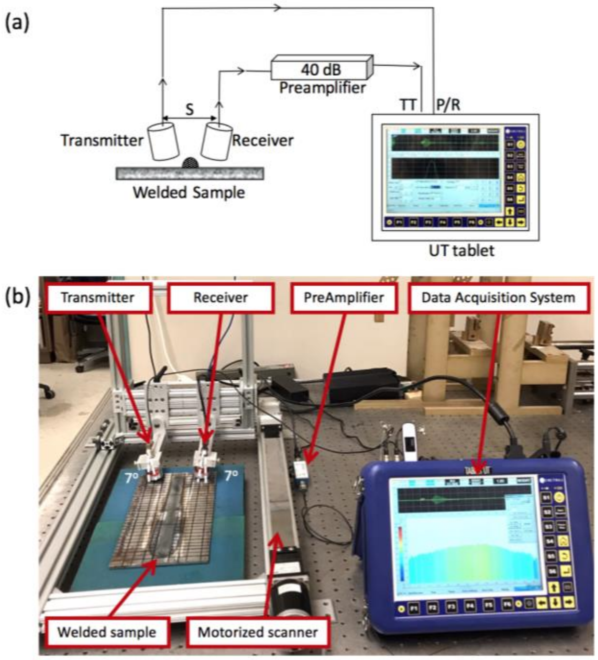

Figure 12 The experimental setup of air-coupled ultrasonic testing: (**a**) schematic; (b) photograph.

A portable dual-channel tablet UT manufactured by Mistras Group (Princeton Junction, NJ, USA) (with a sampling frequency of 100 MHz) was used to generate a two-cycle tone burst signal. First, the excitation signal was amplified with a gain of 52 dB (with a voltage amplitude of 400 volts), and then received through a preamplifier (designed by Mistras Group) with a gain of 40 dB to address the poor energy transfer of the air-coupled transducers, as the transmission loss from air to steel is approximately −45 dB. To improve the signal to noise ratio, 200 waveforms were averaged and filtered with a pass-band of 0.2–10 MHz.

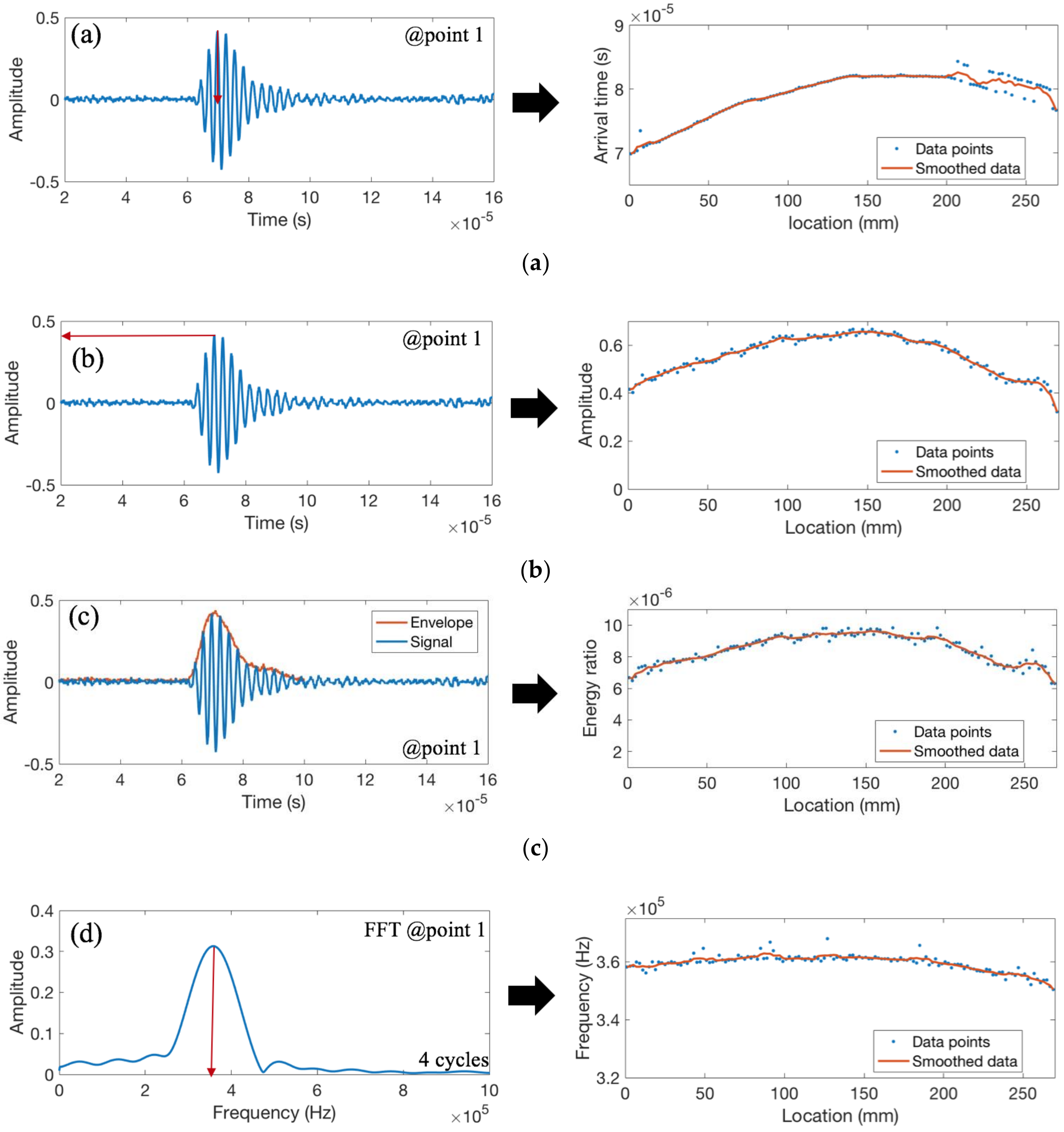

(**a**)

(**b**)

(**c**)

(**d**)

Figure 13 The recorded waveform and features extracted from weld coupon corresponding to (a) the arrival time of the peak amplitude; (b) the peak amplitude; (c) the area under the envelope of the first arrived waveform; and (d) the peak frequency.

Figure 13 shows the recorded waveforms and the extracted features for weld coupon with burn-through defect at the end of sample. Figure 13a shows the arrival time of the peak amplitude along the weld length. It is worth noting that the start and the end of the weld should be disregarded due to inconsistencies caused by the arc start and extinguishing of the arc at the end of the weld. The first part of the weld has insufficient penetration and the final part of the weld has excessive penetration. The sound weld is in the middle section (approximately 100–200 mm length). When there is insufficient penetration, the ultrasonic wave needs to go through two different materials—the base metal and the weld metal—which causes changes in arrival time due to the different properties and interfaces. When there is sound weld, the major part of the ultrasonic signal passes through the weld metal. The results show a sudden increase in the arrival time at the onset of the defect (at location 200 mm), which demonstrates a decrease in the velocity. This can be caused by irregularities in the wave path and/or partial Lamb mode conversions in the weld area. Figure 13b demonstrates the peak amplitude along the weld length, and Figure 13c shows the energy ratio feature calculated using the area under the envelope of the first arrived waveform. Both features (the energy ratio and peak amplitude) decrease with the increase of burn-through defect. The frequency shift feature (Figure 13d) is the frequency of the maximum amplitude calculated from the FFT (fast Fourier transform) of the first four cycles of the waveform. The frequency (decreasing as the weld width increases) is not the result of a shift in the wave propagation frequency but due to the attenuation effect and/or partial wave conversion at the interference of the base metal and the weld metal.

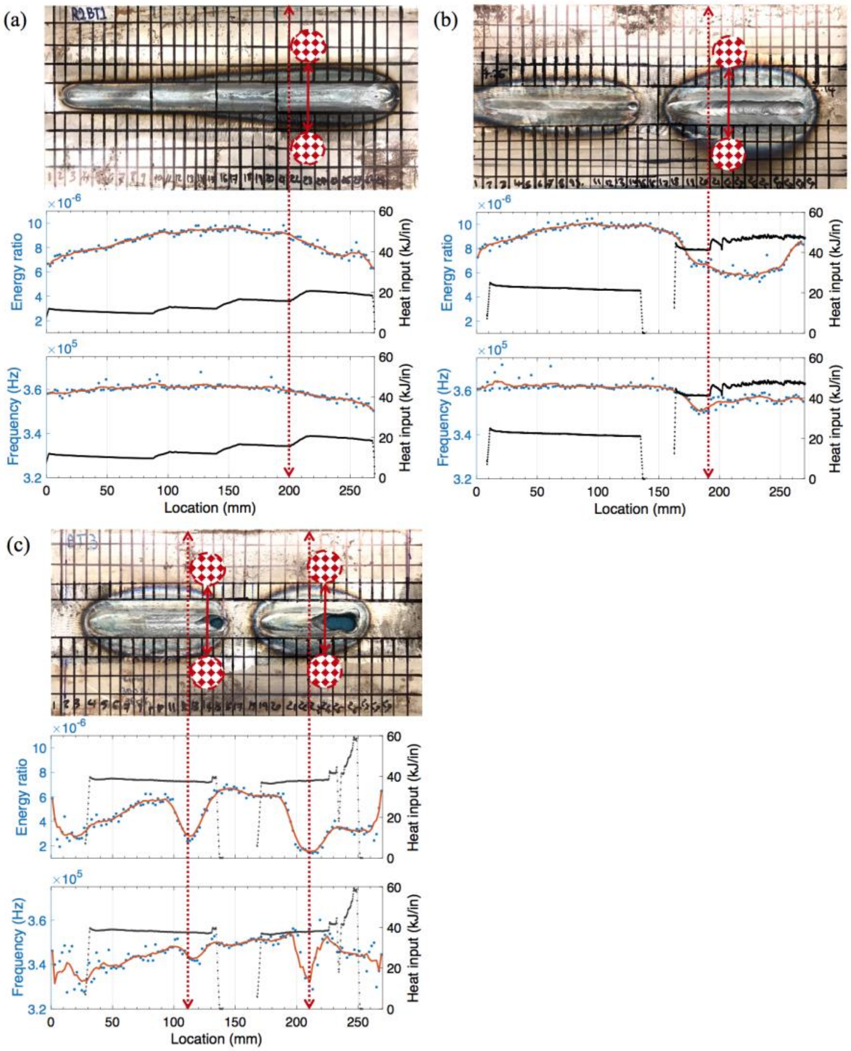

Figure 14 The correlation of UT features (energy ratio and peak frequency) and weld heat input with major changes in the weld microstructure corresponding to weld coupons (**a**) No. 1, (**b**) No. 2, and (**c**) No. 3, respectively.

For weld coupon, there is no open hole; however, excessive penetration is observed towards the end of the plate. Irregularities in the weld metal cause the scattering of ultrasonic waves, reducing the ultrasonic amplitude as well as causing inconsistent arrival time readings. In particular, the A_o mode is more sensitive to changes in the through thickness as it represents the flexural mode where the particle movement is perpendicular to the direction of wave propagation.

Figure 14 shows the correlation of UT features (energy ratio and peak frequency) and weld heat input with significant changes in the weld microstructure. Energy ratio was selected to represent the time domain information as it includes both amplitude- and frequency-related characteristics within its calculation. For all the samples, the energy ratio and frequency values decrease with an increase in burn-through damage (see the dashed red lines on the plots). Energy ratio is more sensitive to weld size and penetration depth. For instance, the energy ratio increases with an increase in weld size and penetration, and then decreases with the presence of burn-through in sample No. 1 and No. 2 as observed at up to 150 mm of weld length. The frequency is only sensitive when burn-through damage is observed. The frequency value decreases below 360 kHz when burn-through damage occurs, which can be explained by the scattering of ultrasonic waves due to discontinuities in the microstructure and partial Lamb mode conversions. For sample No. 3, the energy ratio ($<6 \times 10^{-6}$) and frequency (<350 kHz) are the lowest due to the high current and complete burn-through damage throughout the weld. Two UT features can be used to identify burn-through damage and the welding parameters leading to burn-through damage.

In order to validate the experimental result that changes in the UT features are due to weld penetration, numerical models that take into account the weld morphology and base plate were developed. The microstructure changes of the weld with respect to base metal were simulated by changing the materials properties; while the macro-structure changes were simulated by changing the weld morphology, which was defined by the penetration depth and width. The weld morphology varies depending on heat input. Based on the micrographs obtained from the welded samples, the weld morphology was assumed to be parabolic in shape. The width, and depth measured from the micrographs were used to define the properties of parabolic curve. The mechanical properties of melted zone change due to high temperature. Two different values of Elastic modulus for melted region were defined. The first scenario follows this procedure: the equations of elastic properties as a function of temperature (Young's modulus, $E(T)$ and Poisson's ratio, $\upsilon(T)$) can be found in literature. In the numerical models, the properties of weld were calculated under 350°C:

$$E(T) = e_0 + e_1 T + e_2 T^2 + e_3 T^3$$

$$\upsilon(T) = n_0 + n_1 T + n_2 T^2 + n_3 T^3 + n_4 T^4$$

where, $e_0 = 206\ GPa$, $e_1 = -0.04326\ GPa/C$, $e_2 = -3.502\ \times 10^{-5}\ GPa/(C)^2$, $e_3 = -6.592 \times 10^{-8} GPa/(C)^3$, $n_0 = 0.2874, n_1 = 2.5302 \times 10^{-5}\ n_2 = 2.6333 \times 10^{-8}, n_3 = -9.94196 \times 10^{-11}$, $n_4 = 1.26178 \times 10^{-13}$.

The second scenario was based on the hardness measurement, see in Figure 15. Hardness is a measure of how resistant a material is to permanent shape change, which depends on ductility, elastic stiffness, plasticity, strain, strength, toughness, viscoelasticity and viscosity. The microhardness measurements were conducted across BM, HAZ and melted region. Five measurement points were selected along BM-HAZ-melted region. The largest hardness is measured in HAZ, while the hardness in melted region is 16.5% higher than that the one in BM. According to Peng et al (2018), the Elastic modulus at HAZ is less than the Elastic modulus of base metal while the hardness of HAZ is higher than the hardness of base metal. Therefore, Young's modulus of 190 GPa in the melted region was obtained. The material properties in the numerical model is summarized in Table 5.

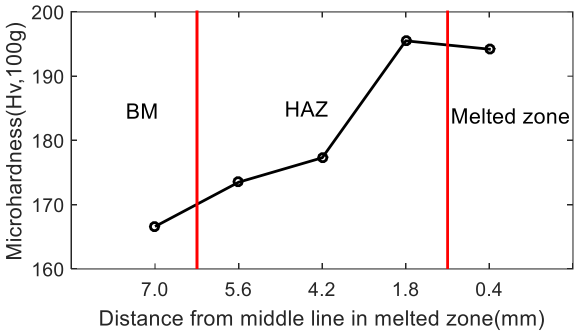

Figure 15 The microhardness results

Table 2. Materials properties of different components in numerical model

Property	Base metal (A36 steel)	Angled wedge (Acrylic plastic)	Melted region
Elastic modulus (GPa)	206	50.8	160/190
Density (kg/m3)	7850	1160	7850
Poisson's ratio	0.26	0.34	0.29

Five different weld morphologies were simulated as shown in Figure 16. The details of width and depth of the melted zone are shown in Table 3. The weld morphologies 1 to 5 correspond to the different weld penetration. The excitation signal with the same frequency and cycles as the experimental setup was applied as a line load at the transmitter location, see in Figure 16. The incident angle was changed according to the excitation frequency similar to experiments. The displacement response of radial direction was collected from the receiver position.

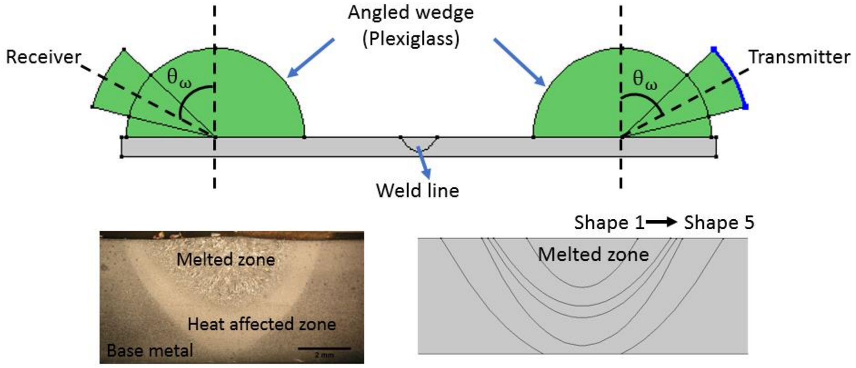

Figure 16 The schematic of numerical simulation.

Table 3. The welding pool shape.

Weld morphology	Weld width (mm)	Penetration depth (mm)	Area (mm^2)
1	4.6	2.0	7.4
2	7.4	2.8	15.5
3	7.9	3.3	19.3
4	8.4	4.4	25.7
5	11.8	4.8	44.9

Waveforms obtained from experiment and numerical models for the weld morphology 1 are compared in Figure 17. Though differences between numerical and experimental signals exist, overall trends in waveforms and frequency spectra agree with each other. The main differences can be attributed to numerical simplifications, such as, (a) transducers and couplant were not taken into account; (b) plane strain approximation was used; and (c) mechanical properties of melted region were taken from literature. However, the purpose of numerical model is to illustrate the influence of weld profile to UT energy ratio. The energy ratio was extracted from numerical models and compared with the experimental results in Figure 18. The increase of weld penetration causes the decrease of UT energy, similar to experimental results. Higher dissimilarity in materials properties introduces higher difference in the UT energy. The experimental result fits into two contrasts of Elastic modulus ratios (base metal/melted region). The numerical results confirms that the dependence of LUT energy ratio and frequency to the weld morphology.

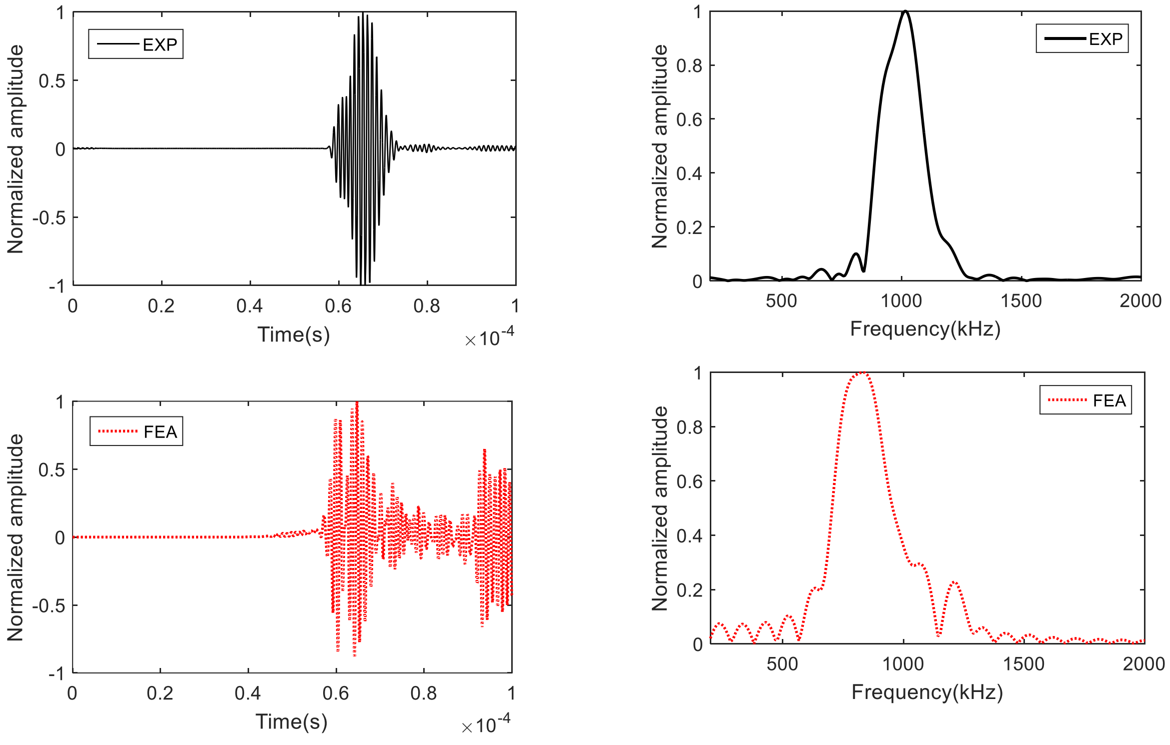

(a) (b)

Figure 17 The comparison of experimental and numerical results (a) time history signals and (b) their frequency spectra.

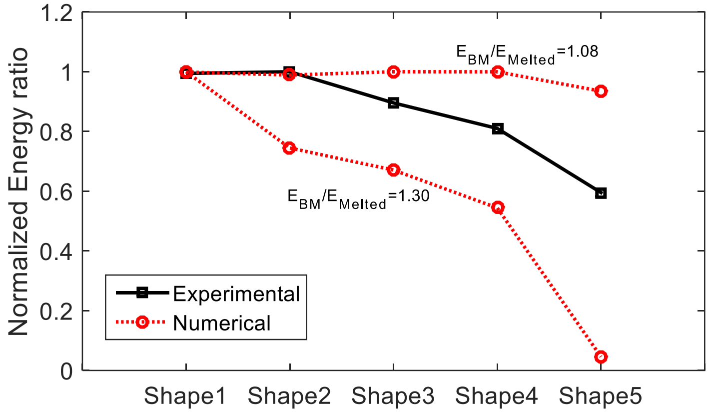

Figure 18 The comparison of numerical and experimental results of energy ratio.

AE Features for GMAW: In addition to TDD data, GMAW produced significant HDD data. From the transient AE signal, AE features such as amplitude, count, frequency centroid are extracted. Figure 19 shows an example of AE signal and AE features extracted from time domain and frequency domain.

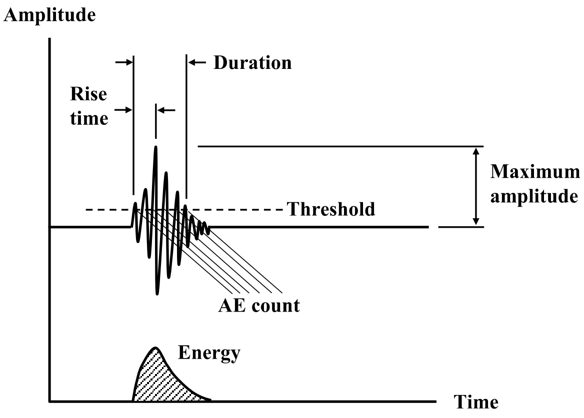

- Amplitude
- Energy
- Duration
- Counts
- Rise time
- Counts to peak
- ASL
- RMS
- Average frequency
- Initiation frequency
- Reverberation frequency
- Absolute energy
- Frequency centroid
- Peak frequency
- Partial Powers

Figure 19 Typical AE signal obtained from HDD and AE features.

After analyzing all the features, amplitude, frequency centroid and count are identified as two major HDD features correlated with the weld state. Figure 20 shows amplitude versus frequency centroid, and amplitude versus count scatter plots from three representative data sets. It is concluded from the figures that differences in AE features among good weld, burn-through and porosity are observed well using amplitude, frequency centroid, and count. These HDD features are utilized in the machine learning algorithm of GMAW.

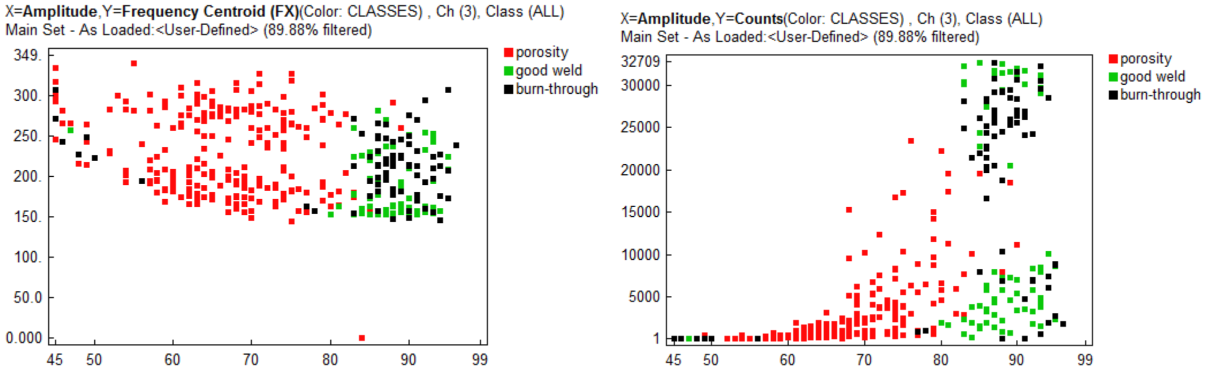

Figure 20 Scatter plots representing good weld, burn-through and porosity obtained from John Deere data.

UT Features for GMAW: The ultrasonic measurement consists of linear and nonlinear ultrasonic testing (LUT and NLUT). The experimental setup for both methods is similar: two normal beam transducers from Olympus were used in through-transmission mode; in which, two 1 MHz transducers were transmitters and receiver for LUT, respectively; and 500 kHz transmitter and 1 MHz receivers were used for NLUT. In order to introduce a refracted shear wave into the weld plate, the plexiglass ultrasonic wedge was set as 57^{o} for both LUT and NLUT. Figure 21 shows the experimental setup. Two transducers were placed perpendicularly across the weld line with the constant space of 102.5 mm. The light lubrication oil was used as couplant. In order to reduce the coupling error, a constant weight was applied. Moreover, each measurement was repeated six times with recoupling the transducers to guarantee the repeatability and the measurement error due to coupling. A portable dual-channel tablet UT manufactured by Mistras Group was used as data acquisition system. 10-cycle and 16-cycle tone burst signals with 200-volt amplitude were generated as the excitation signals for LUT and NLUT, respectively. The data acquisition variables were sampling frequency as 100 MHz, digital filter as 200-2000 kHz and average of 200 waveforms to improve the signal to noise ratio. Based on the results obtained from GTAW, the UT energy ratio was extracted and averaged from the scanned area.

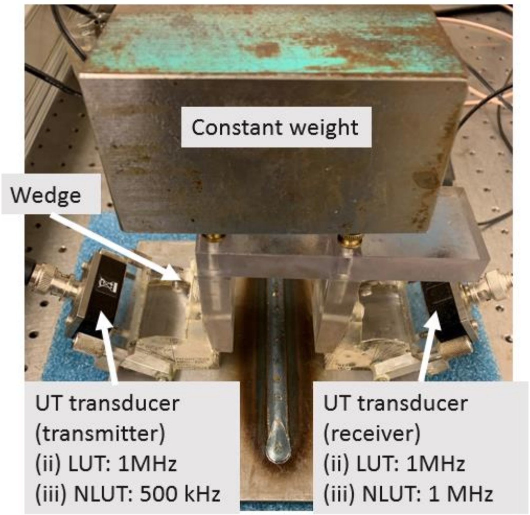

Figure 21 Experimental setup of GMAW UT testing.

The cross section of welding pool was examined by using a stereomicroscope (Carl Zeiss group, Oberkochen, Germany). Figure 22 shows cross-sectional fusion zone (FZ) from GMAW. As shown in Figure 22 (f), the typical morphology of FZ in GMAW consists of bead height (BH) area, bead penetration (BP) area, burn-through. With the increase of weld heat input, the penetration, width and area of FZ increase. The bead height changes less than bead penetration with increment of weld heat input. The weld heat mostly acts on the bead penetration area. Eventually, for P6, burn-though defect was observed. The detailed measurement of FZ with its weld heat input is summarized in Table 4 and their correlations are illustrated in Figure 23. The morphology of fusion zone depends on gun angle, direction of travel, electrode extension (stickout), travel speed, thickness of base metal, wire feed speed (weld current), and voltage. In this project, only weld heat input due to different wire feed speed was changed. The weld width and BP were increased with the weld heat input, leading the increase of FZ. Moreover, a linear function perfectly fits to the measurement, see in Figure 23 (c). The correlation coefficient R^2 is 0.9897. A linear relationship between weld processing variable and FZ forms.

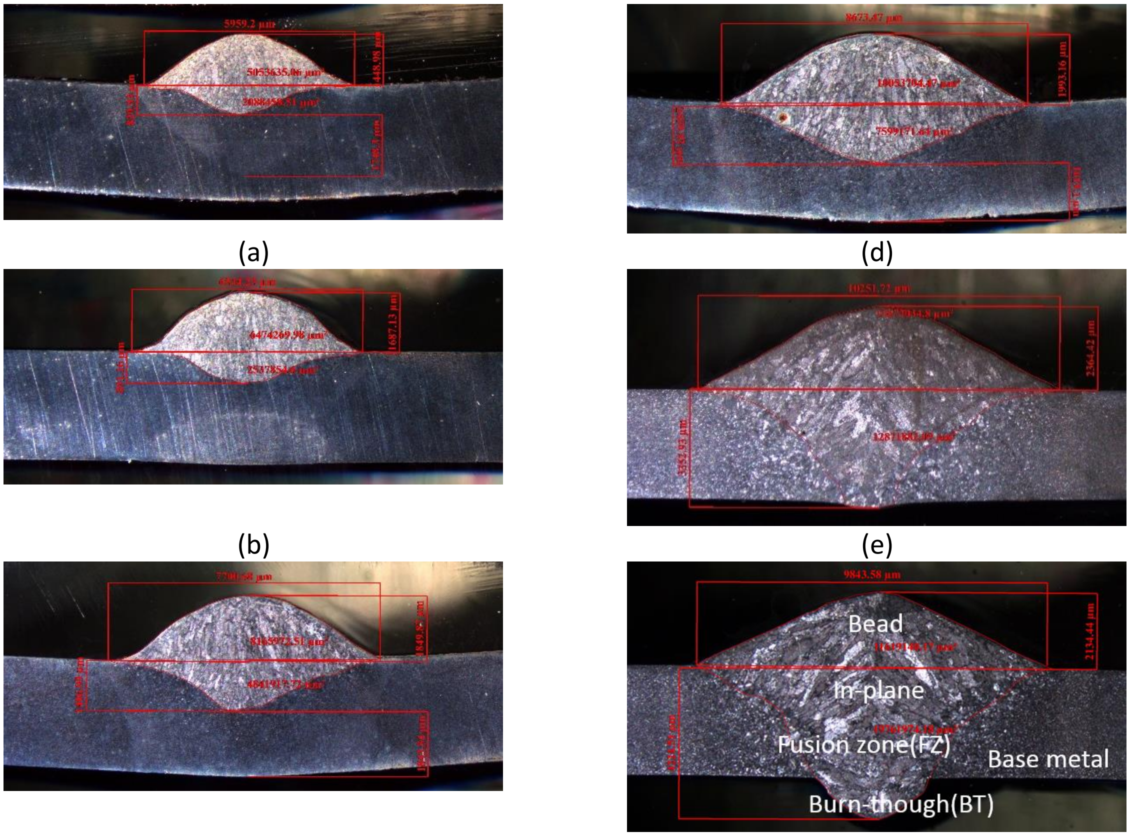

(a) (d)

(b) (e)

(c) (f)

Figure 22 The cross sections of the weld morphology (a) P1 (b) P2 (c) P3 (d) P4 (e) P5 (f) P6.

Table 4 The summary of FZ dimension.

Sample name	Width (mm)	Bead height (BH) (mm)	Bead penetration (BP) (mm)	Area of fusion zone (mm^2)	Weld heat input (kJ/mm)
P1	5.96	0.45	0.83	7.14	0.18
P2	6.54	1.69	0.89	9.01	0.20

P3	7.70	1.85	1.41	13.01	0.30
P4	8.67	1.99	1.66	17.65	0.38
P5	9.27	2.18	3.56	26.54	0.49
P6	9.84	2.13	4.22	31.38	0.58

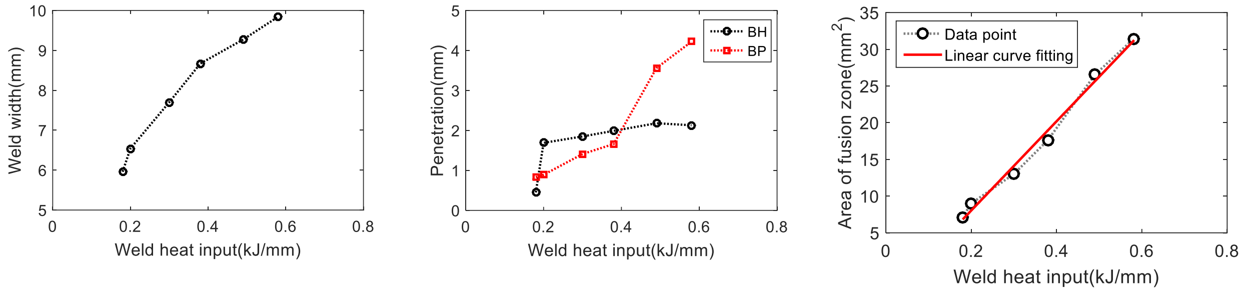

(a) (b) (c)

Figure 23 The relationship between weld heat input and (a) weld width, (b) penetration, and (c) area of fusion zone.

Though the correlation of weld heat input and macrostructure is established, weld is a complex process; therefore, other factors influence the weld penetration as well. Therefore, the UT measurement is implemented to increase the reliability. The UT energy ratios were calculated using the linear UT signals, and compared with the area of FZ. Figure 24 (a) shows the correlation of UT energy ratio and FZ. For P1 to P4, with the increase of weld heat input, the UT energy ratio increases. But for P5 and P6, the adverse trend is observed. From the aspect of the observation, this trend may be caused by the full penetration of the thickness, as shown in Figure 24 (a). The interface due to FZ in P5breflects and dissipates more UT energy, which cause drop of energy. The results of NLUT are shown Figure 24 (b). The nonlinearity parameter (β') reflects the microstructural changes. Heterogeneities in material result in higher β' value, see in Figure 24 (b). With the increase of area of fusion zone, the β' value increases. But for P6, the β' value decreases, which may be due to the presentence of burn-through. Though β' value is correlated with FZ, it is not just the indication of FZ. It reflects the combination of microstructural changes in FZ and HAZ.

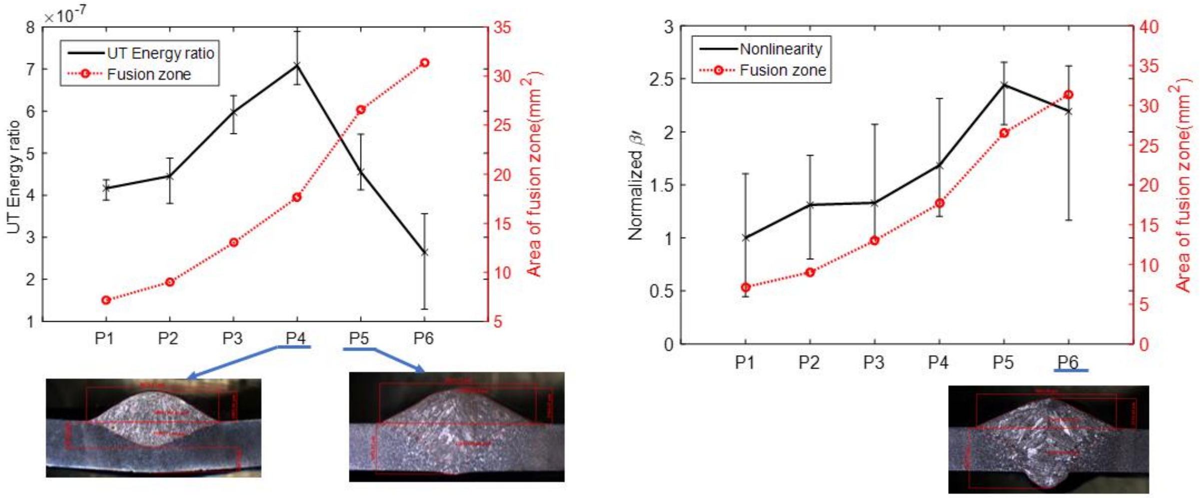

(a) (b)

Figure 24 The correlation of area of fusion zone with (a) UT energy ratio using the 1 MHz transducers, (b) the normalized relative acoustic nonlinearity coefficient.

To validate the experimental results, the numerical models were built. Most of experimental details were preserved in the model, such as loading, geometry and wedge. The geometry information of FZ was extracted from microscopic observation (see in Figure 22) and imported into the numerical model (see in Figure 25). The COMSOL Multiphysics software was used to understand the ultrasonic wave propagation in time domain. In order to reduce the computational time, 2D plane strain approximation was adopted. The pressure wave and shear wave speeds were specified to simulate the wave propagation. The material properties in FE model were presented in Table 5. The wave speed in weld FZ was influenced by the microstructure.

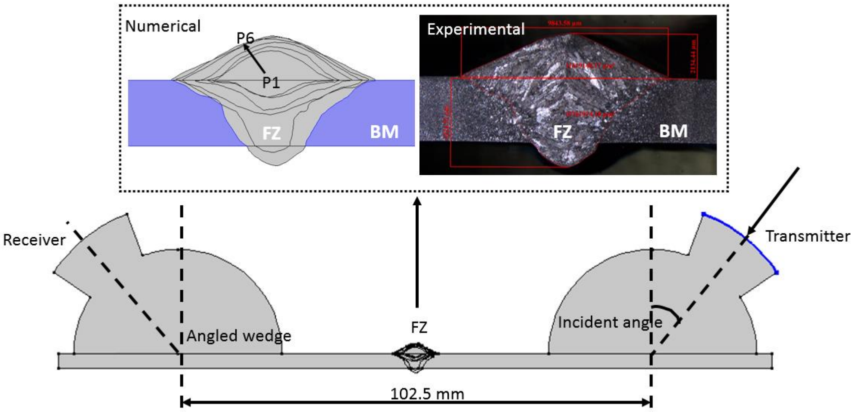

Figure 25 The schematic of numerical model.

Table 5 Materials properties of different components in numerical model.

Property	Base metal	Angled wedge (Acrylic plastic)	FZ
Pressure wave speed(m/s)	5940	7500	7500
Shear wave speed(m/s)	3240	3750	1120
Density (kg/m3)	7800	7850	1160

The waveforms of the experimental and numerical results are compared in Figure 26. Though differences between numerical and experimental waveforms exist, overall signal shapes agree with each other. The main differences can be attributed to numerical simplifications, such as, (a) transducers and couplant were not taken into account; (b) plane strain approximation was used; and (c) the approximate mechanical properties were used. The UT energy ratios were extracted from the numerical data, and compared with the experimental measurement, see in Figure 27. With the increase of FZ, the UT energy increases; however, the UT energy starts to decrease when the full penetration occurs. It is concluded that the UT energy ratio is correlated well with the weld morphology. It is important to emphasize that the numerical model can track the experimental observation, which means that a large data set can be established to understand the influence of different weld morphologies to ultrasonic signal. This overcomes the limitation of data-driven approach where the generation of experimental samples representing a large volume of variables is difficult, time consuming and expensive.

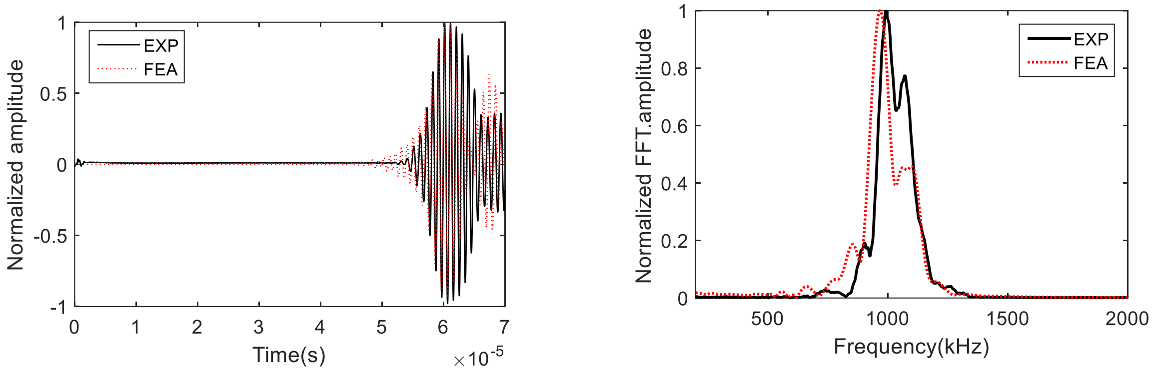

(a) (b)

Figure 26 The comparison of experimental and numerical results from P4 (a) time history signals, and (b) its frequency spectra.

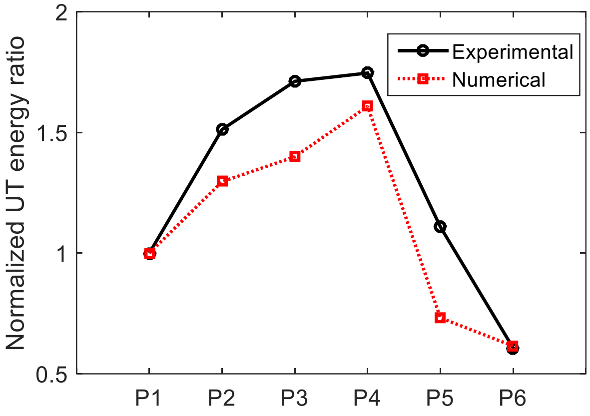

Figure 27 The comparison of numerical and experimental UT energy ratios.

Task 2. Miniaturized Sensor Development

The milestone of this task was the combined MEMS ultrasonic, acoustic emission and temperature sensors with performance comparable to conventional sensors. As a result of this task, new MEMS device is designed, manufactured and characterized. The device accommodates two AE sensors tuned to 40 kHz and 200 kHz, one UT array tuned to 1 MHz and piezoresistive sensor that can function as temperature sensor. The detailed characterizations of AE and UT sensors are completed. While the sensors function as designed, their packaging should be improved to make it adaptable to welding process.

Task 2.1 Finite Element Model of Miniature Sensor: With the advancement of micromachining techniques, several studies have been reported on designing AE and UT sensors based on MEMS. The basic principle of MEMS sensors is based on mass-damping-spring system in micro scale. While MEMS AE sensors operate at the resonant frequency of microstructure (typically tuned to 20 kHz and above), MEMS ultrasonic transducers operate above 1 MHz. The main design variable is the resonant frequency of the sensors. The fundamental frequency of each sensor in z-direction is correlated to its modal stiffness and mass by the ratio of $\sqrt{k/m}$. The resonant frequency can be only adjusted by changing the length, width or the geometry of diaphragm and suspending mass, because the material properties and thickness of each layer are restricted by the fabrication process rules. The diaphragm and the suspending mass were simulated in COMSOL Multiphysics software implementing solid mechanics module. The eigenfrequency analysis was performed in order to find the fundamental mode shapes and frequencies. The thickness of the silicon layer is 10 um while the thickness of the AlN and oxide layers are 0.5 um and 1 um, respectively. Since the thickness of the silicon layer dominates in the entire device layers, only silicon layer was used in the models. The material properties of the silicon used in the numerical models are listed in Table 6.

Table 6 Materials Properties of Si And AlN.

Material	Density (kg/m^3)	Young's Modulus (GPa)
Si	2330	156
AlN	3300	320

Generally, a square shape diaphragm has higher fill factor; however, in terms of stress distribution, it does not have uniform stress especially at the edges where high stress concentration can be observed. An octagonal shape diaphragm was sought as the solution, as it is the closest polygon to circle and satisfies minimum beam dimensions of the design rules. The dimensions of the beams and octagonal shapes are listed in Table 7. To design the low frequency sensor, it is needed to have either lower beam stiffness or higher suspending mass. The highest possible size of the beams is restricted by the manufacturing design rules. Therefore, the lower frequency sensor was designed by increasing the suspending mass. The full thickness suspended structures can be defined through the substrate layer of the SOI wafer during the trench patterning procedure. The full thickness suspended mass with octagonal shape is provided during the reactive-ion etching process. The thickness of the mass is the same as the substrate, which is 400 um. The fundamental frequencies of the LF and HF AE sensors and UT sensor obtained from the numerical simulations are presented in Figure 28. The second mode shapes of the sensors are presented as well, which are obtained as 41 kHz, 450 kHz and 2.23 MHz for the LF AE, HF AE and UT sensors, respectively. It is noticed that the first two modes of the LF sensor are close.

Table 7 Dimensions of MEMS AE and UT sensors.

MEMS Sensor	Beam Dimensions (umxum)	Beam Cross Section (umxum)	Octagonal Side (um)	Design Fundamental Frequency	Experimental Fundamental Frequency
Low Frequency (LF) AE	210x215	10x210	210	40 kHz	35 kHz
High Frequency (HF) AE	150x180	10x150	150	200 kHz	175 kHz
Ultrasonic at 1 MHz (UT1)	-	-	200	1 MHz	0.96 MHz

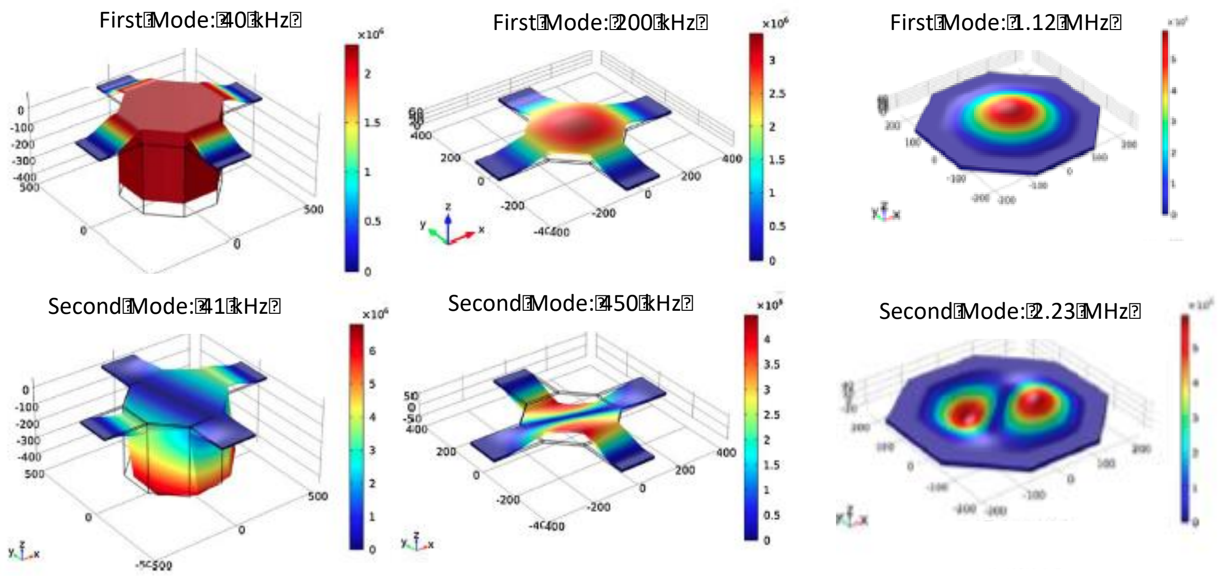

Figure 28 The first and second mode shapes and frequencies for LF AE (left), HF AE (middle) and UT (right) sensors.

Task 2.2 Design and Fabrication of Miniature Sensor: The sensors were manufactured using PiezoMUMPs (Piezeoelectric Multi-User Manufacturing Processes) by MEMSCAP foundry. The PiezoMUMPs method is a 5-mask level SOI (Silicon On Insulator) patterning and etching process, which includes the deposition of 0.5 mm AlN (Aluminum Nitride) to form piezoelectric layer. Figure 29 summarizes the eight main manufacturing steps and the sensor cross sections at each stage. The cross section of MEMS UT sensor is similar to HF AE sensor.

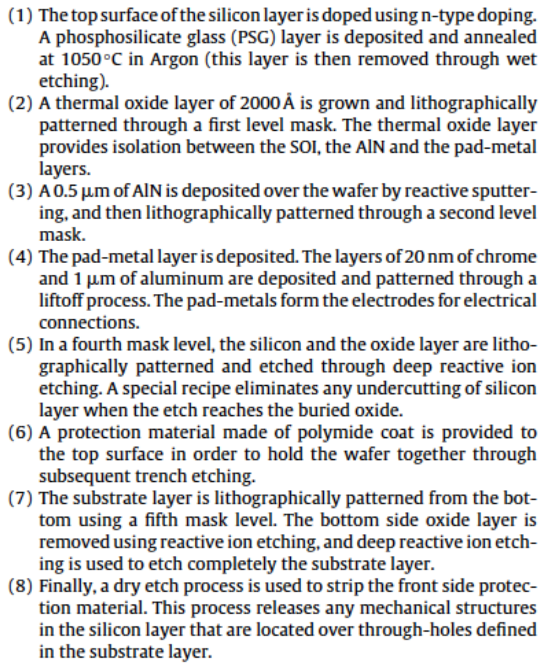

(1) The top surface of the silicon layer is doped using n-type doping. A phosphosilicate glass (PSG) layer is deposited and annealed at 1050 °C in Argon (this layer is then removed through wet etching).

(2) A thermal oxide layer of 2000 Å is grown and lithographically patterned through a first level mask. The thermal oxide layer provides isolation between the SOI, the AlN and the pad-metal layers.

(3) A 0.5 µm of AlN is deposited over the wafer by reactive sputtering, and then lithographically patterned through a second level mask.

(4) The pad-metal layer is deposited. The layers of 20 nm of chrome and 1 µm of aluminum are deposited and patterned through a liftoff process. The pad-metals form the electrodes for electrical connections.

(5) In a fourth mask level, the silicon and the oxide layer are lithographically patterned and etched through deep reactive ion etching. A special recipe eliminates any undercutting of silicon layer when the etch reaches the buried oxide.

(6) A protection material made of polymide coat is provided to the top surface in order to hold the wafer together through subsequent trench etching.

(7) The substrate layer is lithographically patterned from the bottom using a fifth mask level. The bottom side oxide layer is removed using reactive ion etching, and deep reactive ion etching is used to etch completely the substrate layer.

(8) Finally, a dry etch process is used to strip the front side protection material. This process releases any mechanical structures in the silicon layer that are located over through-holes defined in the substrate layer.

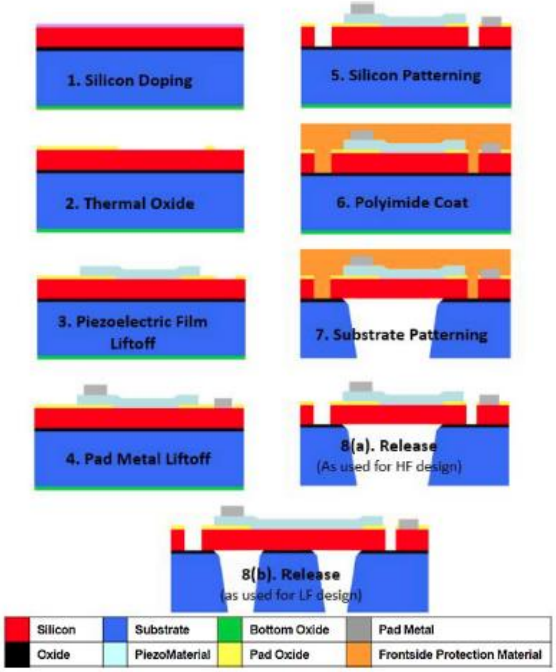

Figure 29 PiezoMUMPs steps implemented in the design of MEMS sensors.

Figure 30b shows the layers and their thicknesses. Planar geometry was modified to tune AE sensors near 40 kHz and 200 kHz and ultrasonic sensor near 1 MHz. Figure 30c shows the final device layout (4 mm x 4 mm area), which also accommodates strain sensor using piezoresistivity property of doped silicon. The UT array was selected to increase signal to noise ratio and phase array applications. SEM images of individual AE sensors are shown in Figure 31.

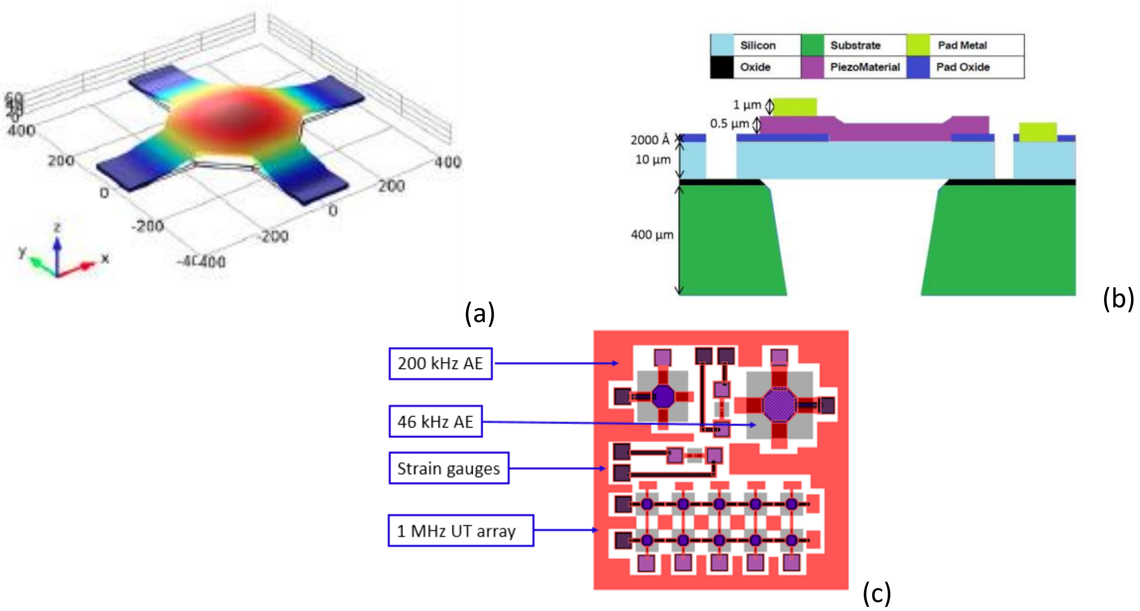

(a)

(b)

(c)

Figure 30 (a) Vibration of silicon diaphragm, (b) sensor layers and materials, and (c) final device layout.

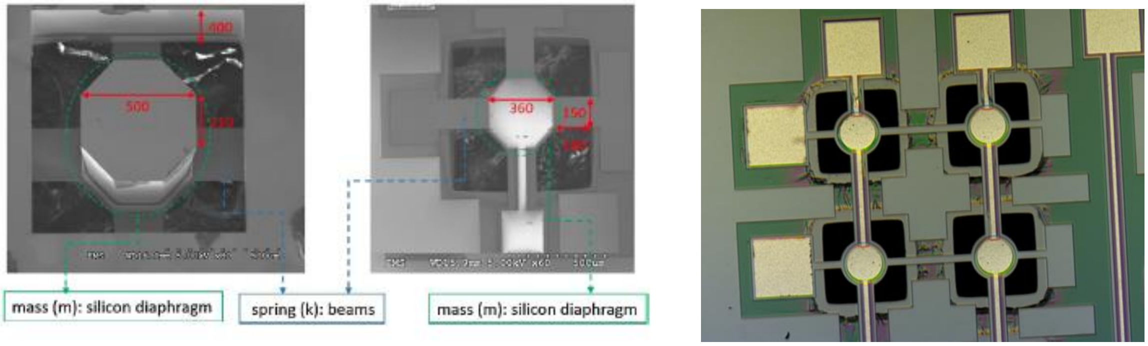

Figure 31 SEM images of LF AE (left) and HF AE (middle), and optical microscope image of UT (right).

Task 2.3 Characterization Experiments of MEMS: After the sensors were manufactured, they were packaged and wire bonded for characterization experiments. The admittance of each sensor was measured using Agilent Technologies 4294A impedance analyzer, which sweeps a range of frequencies and measures admittance. At the resonant frequency of sensor, the admittance is amplified due to electromechanical coupling. Figure 32 shows the results of AE and UT sensors. The resonant frequencies are close to the design values. They also exhibit low damping, which is an advantage to amplify signal and detect only particular frequency. As observed from the numerical models, LF MEMS AE sensor has two resonant frequencies close to each other.

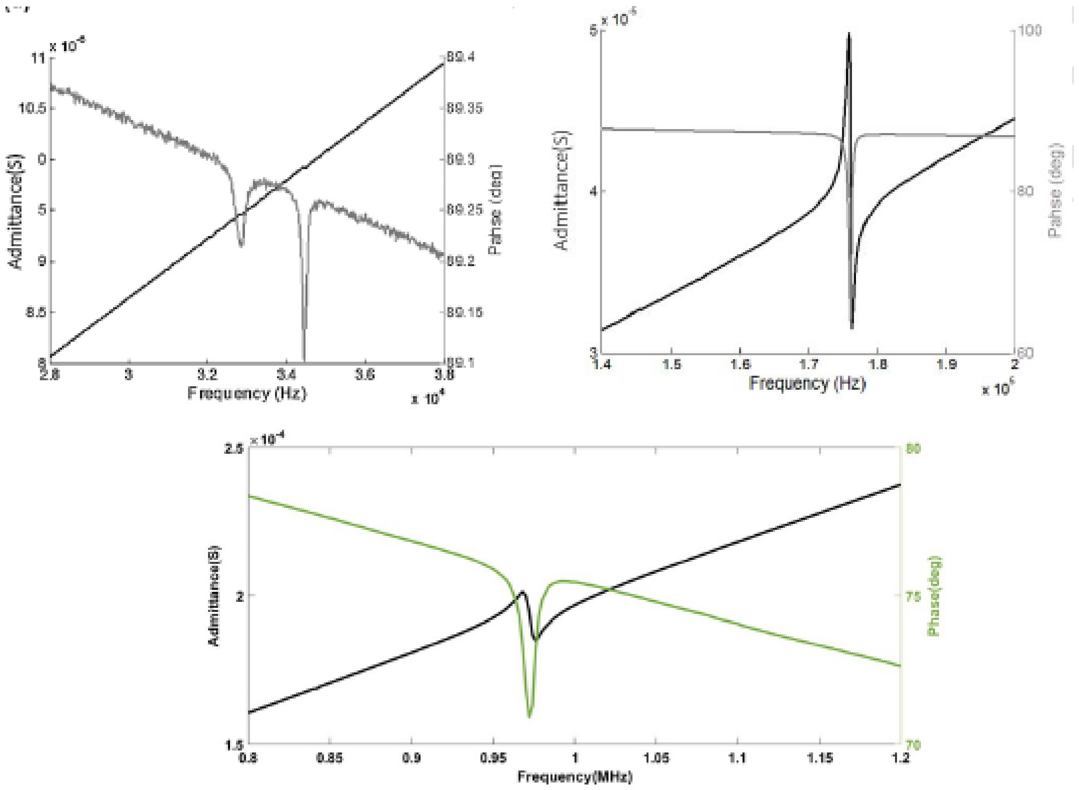

Figure 32 Admittance plots.

Once the sensor functionality was verified with impedance analyzer, the AE sensors were tested using artificially generated source by a conventional piezoelectric sensor as transmitter. The MEMS package was directly attached to the surface of piezoelectric sensor using vacuum grease, Figure 33a. The sensors were connected to the AE data acquisition system manufactured by Mistras Group Inc. A built-in function generator was used to generate 5-cycle, 10 V amplitude sine wave near 170 kHz. The time domain signal and its frequency spectrum are shown in Figure 33b. The piezoMEMS AE sensor has good response at the design frequency near 170 kHz. Due to low damping as observed in the impedance measurement, higher ringing than conventional piezoelectric sensors occurs. This can be reduced by adding backing material or electrical circuitry.

Two MEMS devices were placed face-to-face for testing piezoMEMS UT as transmitter and receiver. Figure 34a shows the experimental setup. The transmitter and the receiver were connected to Ultrasonic data acquisition system manufactured by Mistras Group Inc. They were coupled through air. Silicon and air have matching acoustic coupling coefficient. The receiving sensor was connected to a 40 dB pre-amplifier. The excitation sensor was triggered by 50 V sine wave signal at 1 MHz. Figure 34b shows the received signal and its frequency spectrum. PiezoMEMS UT sensor operates well both as transmitter and receiver.

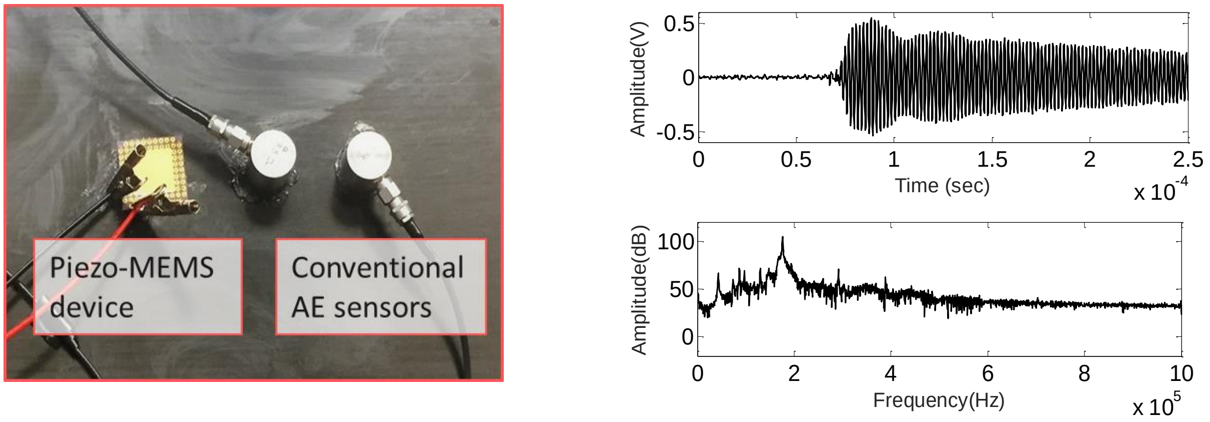

(a) (b)

Figure 33 Simulation experiments of HF MEMS AE, (a) experimental setup, (b) time domain signal and its frequency spectrum.

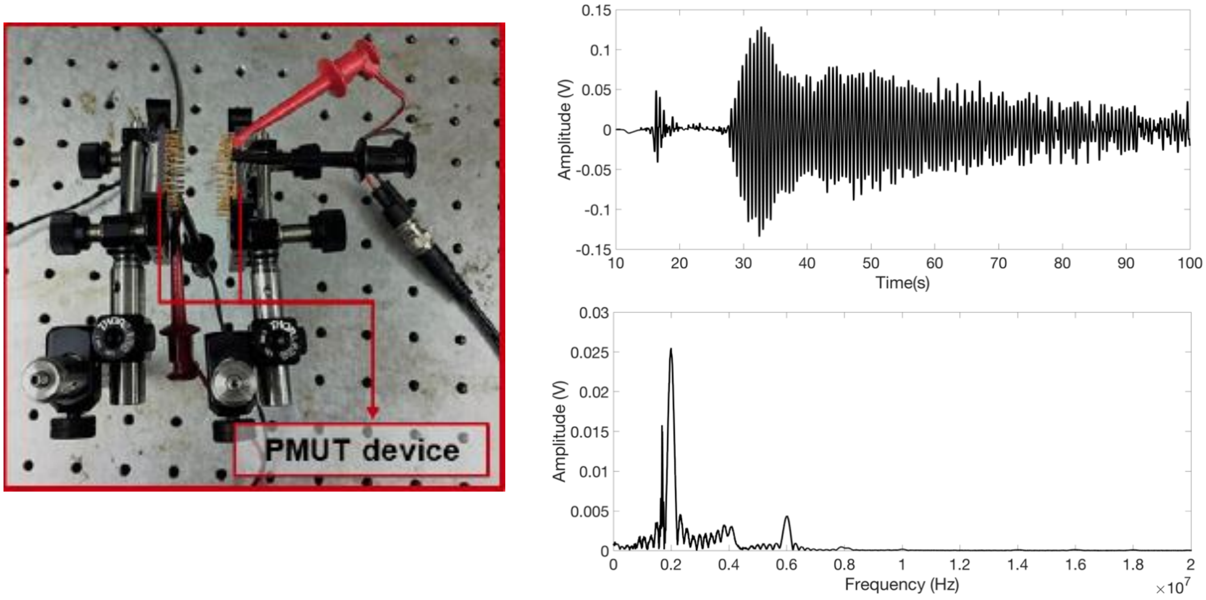

(a) (b)

Figure 34 Simulation experiments of MEMS UT, (a) experimental setup, (b) time domain signal and its frequency spectrum.

Task 3. Electronics Integration

The milestone of this task was the ability to test the prototype in laboratory and field environment. One dimensional scanner was tested both at UIC laboratory and Miller/John Deere laboratories. However, three different data acquisition systems were utilized as different data acquisition parameters were tested to determine the optimal setting. After the optimal setting is determined, all the electronics can be combined into a single system.

Task 3.1 Mechanical dimensions and geometry of scanner: The mechanical scanner was built to track the welding torch such that the distance between weld and sensors would be kept the same. The primary requirements were single axis linear scanner, which can be synchronized with the welding head over a linear distance of at least 12”. A scanner gantry was designed such that mechanically stable holding fixtures for the AE, ultrasonic, and IR temperature sensor could be mounted to the linear actuator and tracking the weld. An additional requirement was to have the stepper motor drive such that it is compatible with the Mistras Tablet UT instrument. The completed design (shown in Figure 35), constructed from T-slotted aluminum extrusions, has dimensions of 16”W x 28”L x 16”H with a linear movement capability of 18”. The “tower” features adjustable 8” of vertical and 7.5” of horizontal movement to aid in precise sensor positioning. The horizontal movement includes a mounting plate with four ¼” through holes for attaching accessories/holding fixtures. Mounting feet were attached at the corners of the gantry and elevate the fixture 1” above the welding table. The feet may be clamped down or permanently attached to the welding table via accessible through holes.

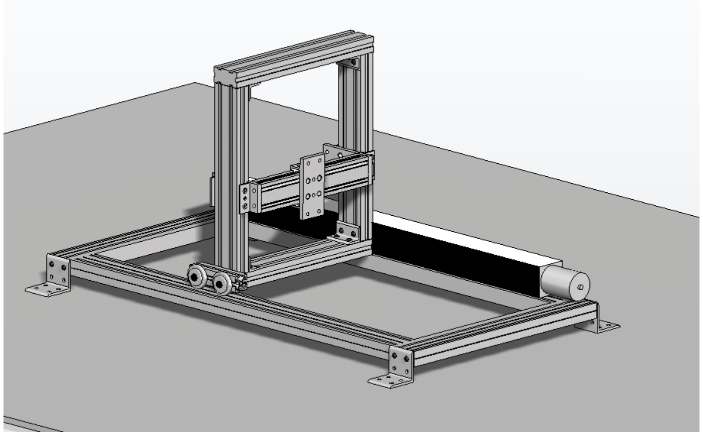

Figure 35 One dimensional scanner.

Task 3.2 Integration of motorized testing capability: A stepper motor was used to control the movement of the tower, which was synchronized with the movement of the welding torch. The initiation of the scan and the speed of the scanner were controlled using the Mistras Tablet UT. The Tablet UT instrument is only capable of sending/receiving control pulses to a motor drive/indexer and is not itself capable of providing drive current. As a result, a standalone drive (Parker/Compumotor ZETA-4 drive) was used to receive the control pulses from the Mistras Tablet UT instrument.

Task 3.3 Integration of sensors: Figure 36 shows the sensor holder design. There are two sliding sensor sub-assemblies each with a fixture for an acoustic and ultrasonic sensor. These are mounted on a slide, which allows the separation between the sensors to be varied by the user. The acoustic sensors are located above the ultrasonic sensor holders and there is a slide, which allows their position to be varied axially relative to the location of the ultrasonic sensor centerline. The vertical height of both sensor sub-assemblies can also be varied. The ultrasonic sensor holder can be angulated to vary the angle between the normal of the sensor and the normal to the weld surface. A mounting scheme has been designed and fabricated for the IR Pyrometer. This scheme allows the Pyrometer to view a spot on the weld nugget at a fixed distance from the welding torch. This approach needs to be adjusted to ensure that there is clear line-of-sight when the UT and AE sensors are mounted.

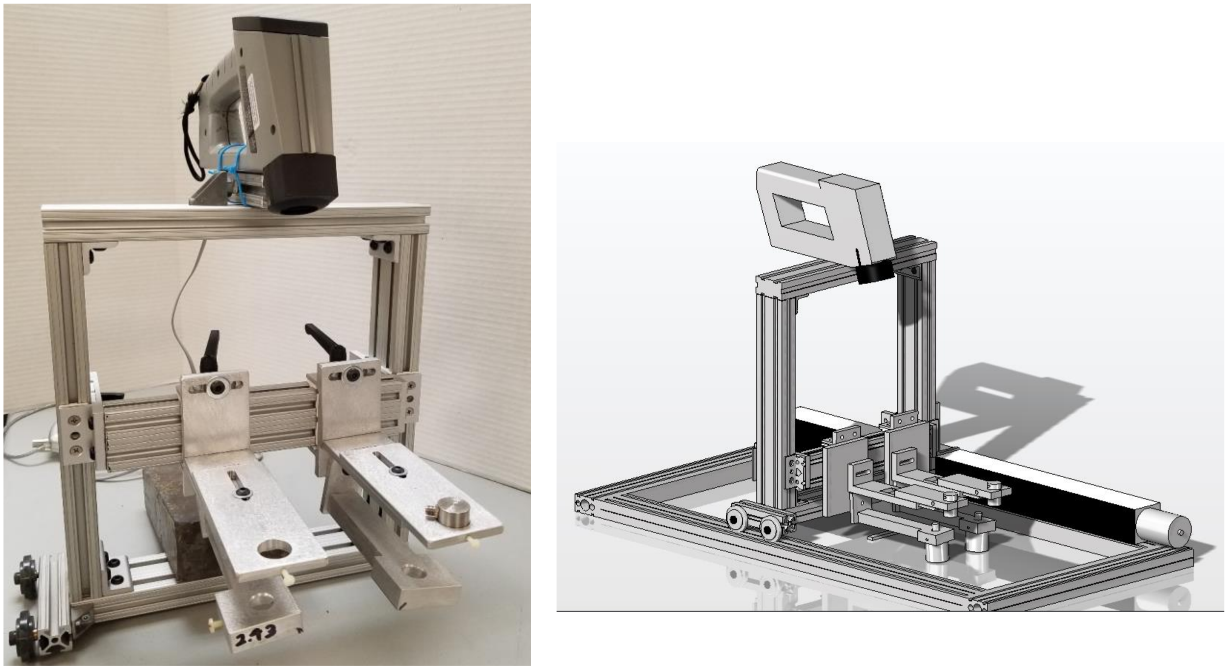

Figure 36 The perspective view of the scanner gantry with the assembled sensor mounting.

Task 4. Field Validation

The milestone of this task was the ability to detect defects induced by welding process and control variables real time. The GTAW algorithm developed at UIC is tested at Miller laboratory. As only variable to conduct welding in this project is heat input, the control aspect is not addressed.

Task 4.1 Generating new samples with different flaws: All the results presented above are based on the data collected from the UIC laboratory. As discussed above, new data is collected from ITW Miller and John Deere laboratories. Using the knowledge accumulated from the UIC data, the machine learning algorithms were applied to ITW Miller and John Deere data. The descriptions of samples can be found at Appendix.

John Deere Data: The automated weld was conducted in the middle of the steel plate (HSLA 350) with the dimension of 15 cm × 15 cm × 0.32 cm (length × width × thickness). The Lincoln ER70S6 wire was used. The weld penetration and porosity were created by controlling the wire feed speed and gas flow rate, respectively. The real-time monitoring system was integrated with an automated GMAW that entailed two components: welding parameter monitoring and AE monitoring as shown in Figure 37. The real-time welding parameters (current, voltage and gas flow) were collected using the ARCAgent 3000P system with the Centerpoint software provided by Miller. The experimental setup was similar to UIC and Miller tests. However, AE data was collected from two additional sensors (R1.5 and R15). The AE data was recorded using PCI-8 data acquisition board manufactured by Mistras Group with four different types of AE sensors which could record the acoustic frequency range between 5-400 kHz, see in Figure 37. Four types of AE sensors were attached to scanner in air-coupled mode: 1 x R6 (resonant type sensor with the frequency range of 35-100 kHz), 1 x WD (wideband type sensor with the frequency range of 100-900 kHz), 1 x R1.5 (low frequency resonant type sensor with the frequency range of 5-20 kHz), and 2 x R15 (narrow band resonant type sensor with highest sensitivity of range of 150 kHz). The major data acquisition variables were the digital filter as 20-400 kHz for R6, 100-400 kHz for WD and R15, and 1-50 kHz for R1.5, which had good frequency range to cover all of the possible AE activity during the weld. The threshold level was set as 45 dB. All of the sensors were connected to 40 dB pre-amplifier. AE waveforms were recorded with 3 MHz sampling rate for WD and R15; for the R6 and the R1.5, the sampling rate was 1 MHz. In order to decrease the error due to the spatial influence, the AE sensors were attached to a motorized scanner. All of the sensing components were synchronized with the speed of the welding torch.

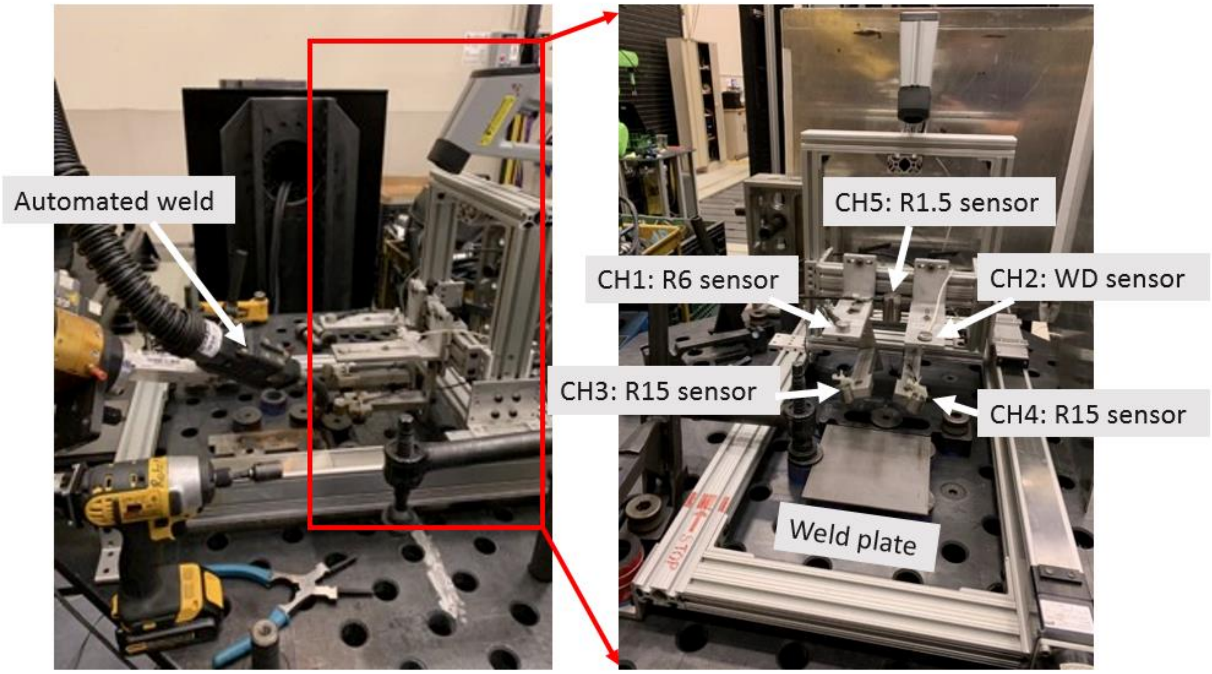

Figure 37 John Deere experimental setup.

During welding, both time driven data (TDD) and hit driven data (HDD) were continuously collected by the AE system; herein, average signal level and absolute signal energy are TDD; while counts, amplitude, frequency centroid, and peak frequency are conventional HDD features. Voltage, current, gas flow rate, traveling speed and wire speed from the weld parameters were also recorded along with AE features.

In order to form representative training set, different levels of penetration and porosity were artificially manufactured. For each case, the same weld was repeated at least three times, two for the training set and one for evaluating the performance of the trained machine learning algorithm. The key controllable variables and expected weld are summarized in Table .

Task 4.2 Identifying the weld flaw with the developed algorithm:

GMAW Data Recorded at John Deere Laboratory: After analyzing the signals, WD and one of the R15 sensors were selected. TDD data was recorded every 20 ms. From those, 200 ms segments / windows were created, from which the average, the minimum, the maximum, and the accumulation rate values were computed. The accumulation rate is the difference between the linear accumulation and the real accumulation (see Figure 38). HDD data that fall into these 200 ms windows were averaged. Heat input was computed from weld parameters and interpolated to match the 200 ms window.

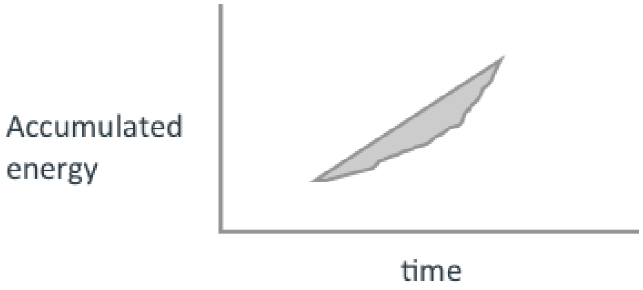

Figure 38 Accumulation energy calculation over time.

First, the features were scaled into the [0, 1] range and then a quadratic transformation was applied. Two machine learning methods were trained and tested. For training, samples 1, 10, 13, 16, 22, 23, 31, and 32 from Table were used. The "class" for the weld qualities are *good* weld, penetration, burn-through with hole, or porosity (see Appendix). Let X_t be the features extracted for time *t*, and Y_t be the class label, then for a model *f* the prediction for each timestep *t* is made as:

$$Y_t = f(X_t)$$

In contrast, a sequence tagging model makes a prediction for the entire sequence as:

$$Y_{1:t} = f(X_{1:t})$$

Logistic Regression (LR) predicts each time step individually by finding the maximum probability of a class:

$$Y_t = \underset{Y_t}{argmax}\ P(Y_t = c\,|X_t;\theta), \quad P(Y_t = c\,|X_t;\theta) = \frac{e^{\theta_c \cdot X_t}}{\sum_{j=1}^{C} e^{\theta_j \cdot X_t}}$$

where $P(Y_t = c\,|X_t;\theta)$ is the probability of Y_t having class c given the features X_t and learned parameter ϑ, and the parameter ϑ is learned by optimizing the following objective:

$$\min_{\theta}\left[\sum_{j=1}^{C}(Y_i = j)\log P\,(Y_i = c|\,X_i;\,\theta)\right]$$

On the other hand, as a sequence tagging model, Adversarial Sequence Tagging (AST) predicts the full sequence utilizing a game-theoretic perspective:

$$Y_{1:t} = \underset{Y_{1:t}}{\text{argmin}}\ \max_{P(Y'_{1:t}|X_{1:t})} E_{P(Y'_{1:t}|X_{1:t})}\left[\sum_{k=1}^{t}(Y_k \neq Y'_k) + \psi(Y'_{1:t}, X_{1:t})\right],$$

where $\psi_\theta(Y'_{1:t}, X_{1:t}) = \sum_{k=1}^{t}\theta.\phi(Y_k, X_k, Y_{k-1})$, is a potential term that motivates Y' to be similar to the training data, $\phi(Y_k, X_k, Y_{k-1})$ is the feature function corresponding to timestep *k* and previous timestep *k-1*. The parameter θ is learned by the objective:

$$\min_{\theta}\ \min_{P(Y_{1:t}|X_{1:t})}\ \max_{P(Y'_{1:t}|X_{1:t})} E_{P(Y_{1:t}|X_{1:t})P(Y'_{1:t}|X_{1:t})P(X_{1:t})}\left[\sum_{k=1}^{t}(Y_k \neq Y'_k) + \psi_\theta(Y'_{1:t}, X_{1:t})\right]$$

Table 8 shows the predictions from the two machine learning models. Here the training samples were excluded. Four of the classes were predicted for each weld samples. The results are shown in percentages of the 200 ms windows per sample. Usually there were 24 to 31 time-windows for these samples.

Table 8 Machine learning predictions.

	Adversarial Sequence Tagging				Logistic Regression			
#	Good	Penetration	Burn Through	Porosity	Good	Penetration	Burn Through	Porosity
2	100	0	0	0	100	0	0	0
3	100	0	0	0	91.89	0	0	8.11
4	100	0	0	0	100	0	0	0
5	100	0	0	0	100	0	0	0
6	100	0	0	0	100	0	0	0
7	100	0	0	0	100	0	0	0
8	100	0	0	0	100	0	0	0
9	100	0	0	0	100	0	0	0
11	100	0	0	0	100	0	0	0
12	100	0	0	0	100	0	0	0
14	0	100	0	0	0	100	0	0
15	0	100	0	0	3.23	96.77	0	0
17	0	27.03	72.97	0	0	75.68	24.32	0
18	0	0	100	0	0	61.29	38.71	0
19	0	0	100	0	0	0	100	0
20	0	0	100	0	0	0	100	0
21	0	0	100	0	0	3.23	96.77	0
24	0	0	100	0	0	0	100	0
25	100	0	0	0	91.89	0	0	8.11
26	100	0	0	0	100	0	0	0
27	93.6	0	0	6.4	80.65	0	0	19.35
28	0	0	0	100	6.45	0	0	93.55
29	0	0	0	100	0	0	0	100
30	0	0	0	100	0	0	0	100
33	2.7	0	0	97.3	2.7	0	0	97.3
34	0	0	0	100	0	0	0	100
35	0	0	0	100	0	0	0	100
36	0	0	100	0	0	0	54.94	45.16
37	0	0	100	0	0	0	61.29	38.71
38	0	0	100	0	0	0	8.11	91.89
39	0	0	100	0	0	0	32.26	67.74
40	0	0	100	0	0	0	67.74	32.26
41	0	0	100	0	0	0	18.92	81.08
42	0	0	96.77	3.23	0	0	19.35	77.42

Figure 39 shows three examples of machine learning algorithm results. The horizontal axis shows the position of weld; the vertical axis shows ASL. The important result from these plots is the percentage distribution of each class, which describes the overall quality of weld. In general, samples 2-12 are all correctly predicted as good welds by AST. LR has minor errors. The excessive penetration samples (14-18) have mixed predictions in both models, but AST leans towards burn-through for latter ones. Samples 19-21 were initiation of burn-through. Those samples had heavy melting and could fall between penetration and burn-through classes, AST classifies all as burn-through. For samples 25-27, the samples did not show any sign of porosity, and in the prediction, their percentages are as expected. However, samples 36-42 had both burn-though and porosity, AST mostly predicts burn through for them, whereas LR predicts mostly porosity for them. If we consider 5% leniency per sample and consider either of the two classes for 19-21 and 36-42 correct, and 25-27 being non-porosity samples, then both models correctly fails in sample 27, but only LR fails in 25 and 3. Both methods label also fails in sample 17-18, which have higher melting in the category. The macro accuracy, i.e. in terms of samples being correctly classified, for AST is then 91.18% and for LR it is 82.35%.

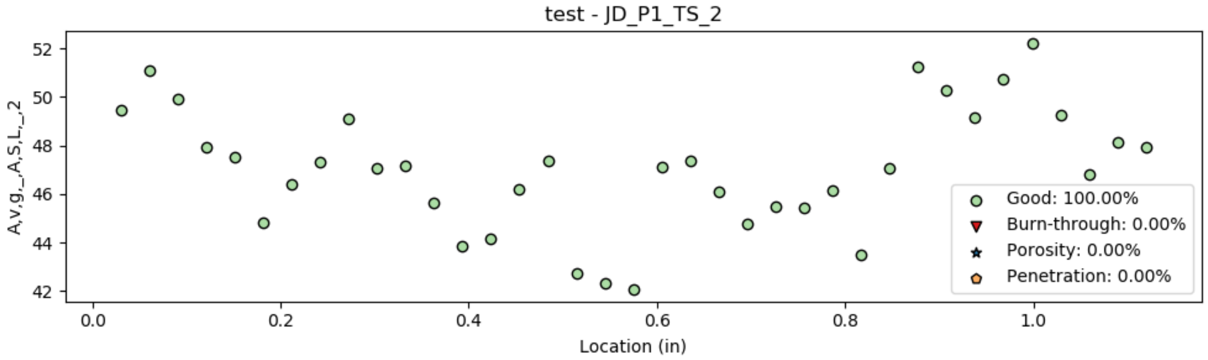

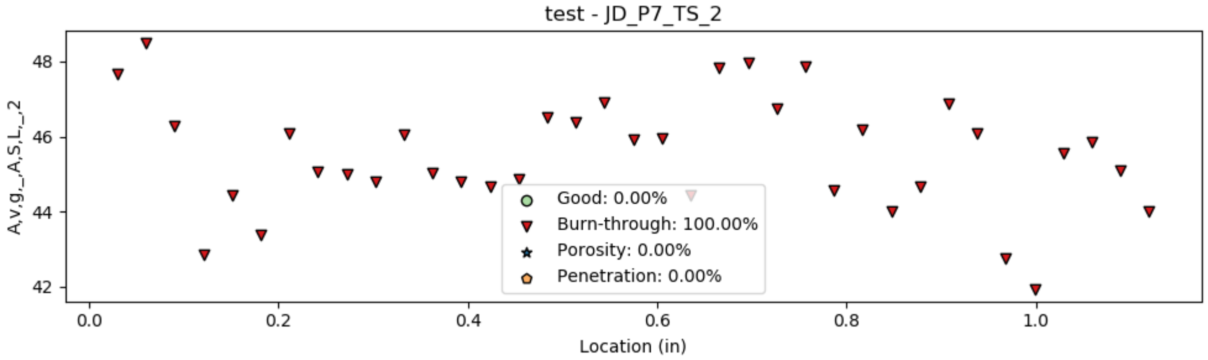

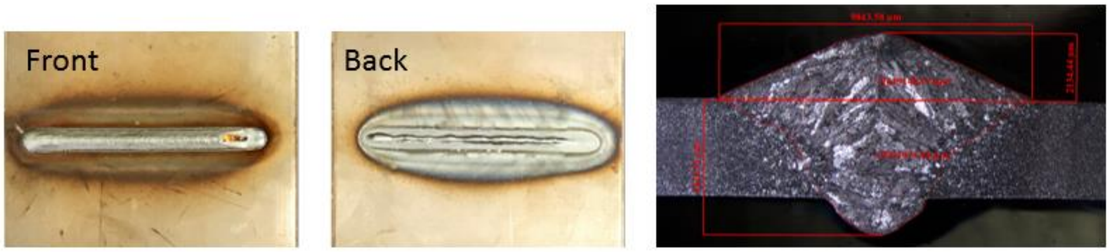

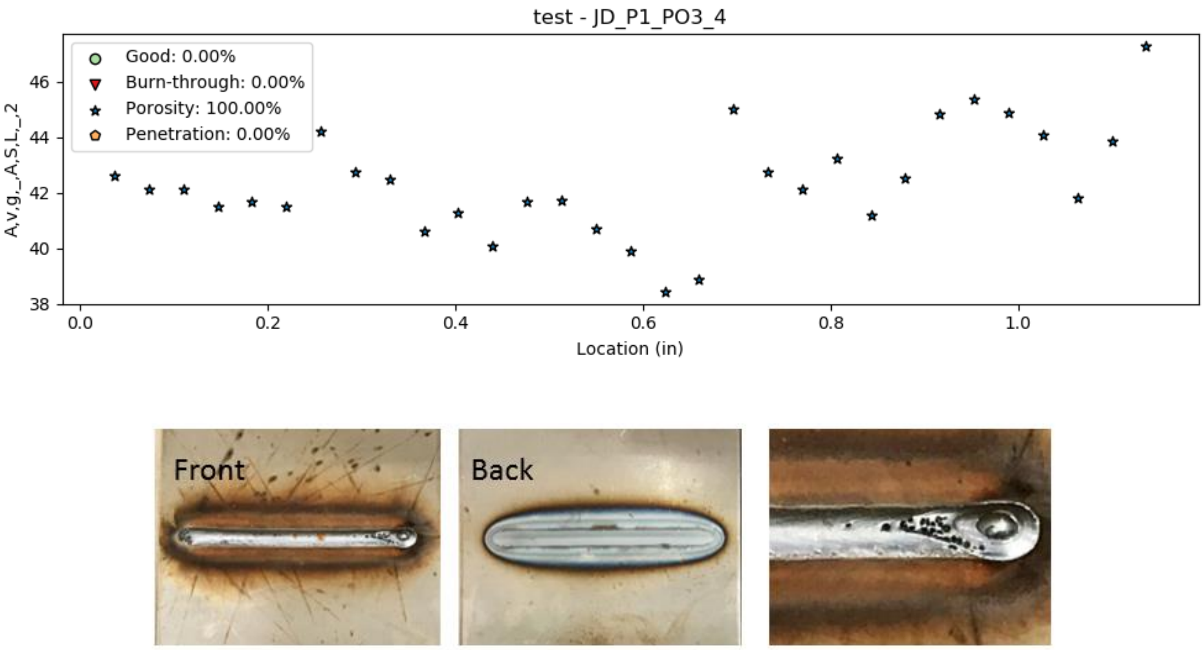

Figure 39 Three examples of machine learning algorithm results for GMAW.

GTAW Data Recorded at UIC and Miller Laboratories: The same algorithm is applied to GTAW samples manufactured at UIC and Miller laboratories. Only difference between GTAW and GMAW algorithm is that no HDD data is used for training and testing sets of GTAW samples. Table 9 shows predictions in GTAW samples. The samples are described in the appendix.

Table 9 GTAW welding experiment results.

Sample		Machine Learning Result		Expected weld state
		Good Weld	Burn-through	
ML1		100.00	0.00	Varies
ML2		50.94	49.06	Varies
ML3		100.00	0.00	Varies
ML4		100.00	0.00	Varies
ML5		100.00	0.00	Varies
S8	1	100.00	0.00	good weld
	2	88.28	11.72	good weld
	3	91.34	8.66	good weld
S9	1	100.00	0.00	good weld
	2	100.00	0.00	good weld
	3	94.29	5.71	good weld
S10	W1	44.93	55.07	Excessive penetration
	W2	10.00	90.00	Burn-through (with hole)
	W3	22.86	77.14	Burn-through (with hole)

S11	W2	94.20	5.80	good weld
	W3	61.24	38.76	Penetration
S12	W1	63.67	36.33	Penetration
	W2	0.00	100.00	Excessive penetration
S13	W1	100.00	0.00	Square groove
	W2	100.00	0.00	Square groove
	W3	100.00	0.00	Square groove

III. KPI'S & METRICS

The key metrics presented in the proposal and the results/validation methods are presented in the following table and described below. Using the current data acquisition systems (for AE, UT and welding), sensors (two AE sensors, two UT sensors, current sensor, voltage sensor and gas flow sensor) and scanner, typical setting time is about one hour. As three different data acquisition systems are utilized, the cost is high. However, as the outcome of this project indicates that AE combined with welding sensors is the ideal NDE method, the cost per welding system to add AE setting, sensor and data acquisition system can be reduced to less than $10k.

Metric 1: Integrated and miniaturized sensor platform – Existing AE and UT sensors are bulky and expensive. To miniaturize the sensors and make them cost effective, MEMS device accommodating AE and UT sensors on 4 mm x 4 mm area is designed, manufactured and characterized. The cost of each device can be less than $10 when mass manufacturing is utilized. All the sensors function as designed. However, it requires robust packaging and electronic shielding suitable to harsh welding environment.

Metric 2: Real-time response algorithm of weld anomalies within the travel speed of welding process – The original scope of project includes the development of real-time response algorithm for GMAW. In addition to GMAW, GTAW process is studied. While GTAW process is acoustically quite process leading to less accuracy in the predictions, GMAW process results in good prediction accuracy utilizing acoustic emission and welding data as well as Adversarial Sequential Tagging algorithm developed by the UIC CS group. The calculated speed of machine learning algorithm is less than typical travel speed of welding, which means that the welding process can be interrupted if the welding quality is not sufficient without ruining significant piece of material.

Metric 3: Prototype weld monitoring tool adaptable to different welding geometries – The scanner is designed to track the welding torch with the same travel speed while it carries AE, UT and thermal sensors. While the current scanner is one dimensional, capturing complex geometries of welded parts require adapting the AE sensors as part of the welding torch.

Metric	Baseline	Goal	Results	Validation Method
Enter Metric	Enter Baseline	Enter Goal	Enter Results	Enter Validation Method
Integrating MEMS acoustic emission (at 20-60 kHz range), ultrasonic (near 1-2 MHz) and temperature sensors on 1 cm x 1 cm device area	MEMS AE and temperature sensors already designed and characterized	Ultrasonic sensor to be integrated with AE and temperature sensors	4 mm x 4 mm device accommodating UT, AE and temperature sensors	Characterization experiments using impedance analyzer and simulation experiments.
Real-time response algorithm of weld anomalies within the travel speed of welding process	Reference-dependent algorithms with extensive testing	Reference-free machine learning algorithms	More than 90% accuracy in prediction	Experiments at John Deere laboratory
Prototype weld monitoring tool adaptable to different welding geometries	Individual sensors, not a unified approach with multiple sensors	Combining multiple sensors on a motor-controlled unit.	UT cannot be conducted real time. Due to complex nature of welding torch movement in robotic welding, AE sensors should attach to welding torch for universal approach	Experiments at three laboratories

IV. TECHNOLOGY OUTCOMES

System Overview: The system includes hardware and software components. The hardware components include a scanner gantry that carries all NDE sensors and welding sensors. AE and UT and welding data are currently recorded using three separate data acquisition systems. The software component includes data integration algorithm and machine learning algorithm written in the Python open source software language. The final report of the trained and tested algorithm is distance versus classification of each measurement as well as confusion matrices representing the percentage of result accuracies for all classes. For instance, Figure 40 shows the output of machine learning algorithm. Considering that the prediction is conducted real time, the welder can notice that after about 0.3 inch welding, the class changes from good weld to burn-through. The welder can stop the process, check the weld quality and vary the welding inputs if needed to correct the weld state. Instead of locating entire welded piece (according to this result, the weld quality for 0.3 inch to 5 inch is not acceptable).

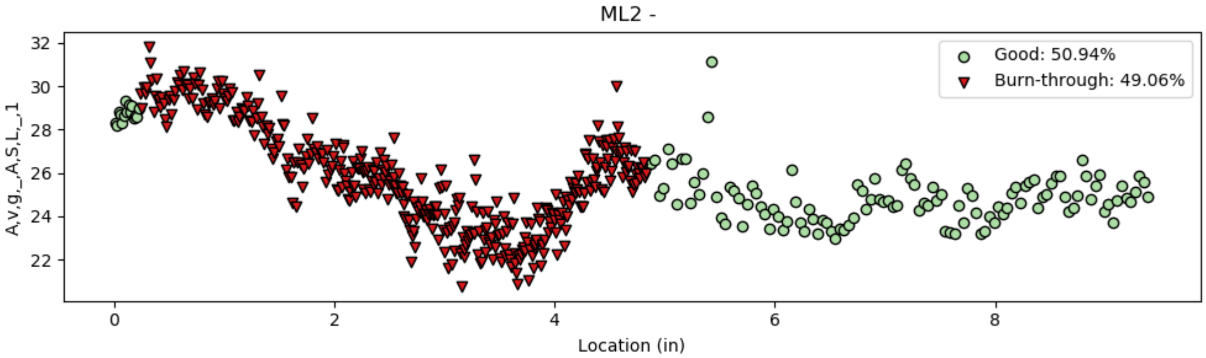

Figure 40 Output of machine learning algorithm.

System Requirements: The primary requirements of scanner gantry are single axis linear scanner, which can be synchronized with the welding head over a linear distance of at least 12”. The scanner gantry is designed such that mechanically stable holding fixtures for the AE, ultrasonic, and IR temperature sensor can be mounted to the linear actuator and track the weld. An additional requirement is to have the stepper motor drive such that it is compatible with the Mistras TabletUT instrument. The completed design, constructed from T-slotted aluminum extrusions, has dimensions of 16”W x 28”L x 16”H with a linear movement capability of 18”. The “tower” features adjustable 8” of vertical and 7.5” of horizontal movement to aid in precise sensor positioning. The horizontal movement includes a mounting plate with four ¼” through holes for attaching accessories/holding fixtures. Mounting feet are attached at the corners of the gantry and elevate the fixture 1” above the welding table. The feet may be clamped down or permanently attached to the welding table via accessible through holes. There are two sliding sensor sub-assemblies each with a fixture for an acoustic and ultrasonic sensor. These are mounted on a slide, which allows the separation between the sensors to be varied by the user. The acoustic sensors are located above the ultrasonic sensor holders and there is a slide, which allows their position to be varied axially relative to the location of the ultrasonic sensor centerline. The vertical height of both sensor sub-assemblies can also be varied. The ultrasonic sensor holder can be angulated to vary the angle between the normal of the sensor and the normal to the weld surface. A mounting scheme has been designed and fabricated for the IR Pyrometer. This scheme allows the Pyrometer to view a spot on the weld nugget at a fixed distance from the welding torch.

The primary requirements of AE system include two AE sensors tuned to low frequency (30-150 kHz) and high frequency (100-1000 kHz). The hit-driven and time-driven data are recorded by AE data acquisition system. The primary requirements of UT system include two air-borne UT transducers tuned to near 300 kHz and angled such that generates the highest amplitude transverse wave mode.

The primary requirements of machine learning algorithm includes a computer capable of running Python 3, with libraries scikit-learn, pandas, numpy, matplotlib, jupyter, and gurobi or cvxopt.

System Architecture: The scanner with sensors and welding sensors are demonstrated in Figure 41. As discussed above three different data acquisition systems are utilized to collect AE, UT and welding data.

The measurement architecture envisioned to include only AE and welding sensors is shown in Figure 42. After AE and welding data are recorded real time, they are integrated such that their time steps are the same. Hit-driven and time-driven AE data are averaged for every 200 ms of measurement. UT data is assessed post-welding for weld penetration measurement.

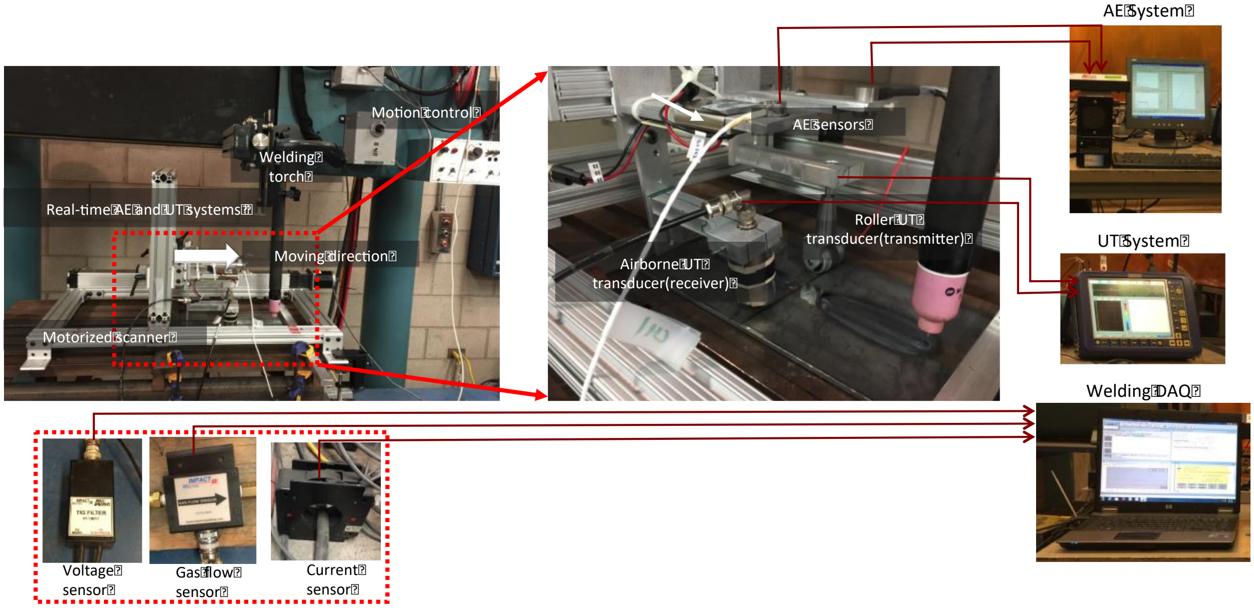

Figure 41 Components of portable welding inspection tool and other welding sensors.

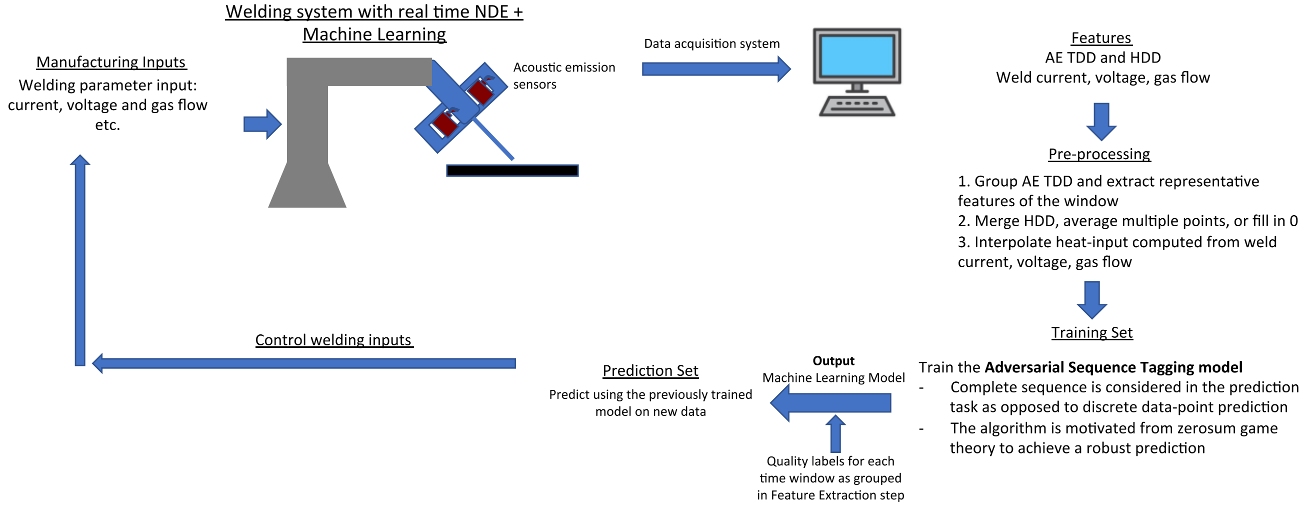

1. Group AE TDD and extract representative features of the window
2. Merge HDD, average multiple points, or fill in 0
3. Interpolate heat-input computed from weld current, voltage, gas flow

Train the **Adversarial Sequence Tagging model**

- Complete sequence is considered in the prediction task as opposed to discrete data-point prediction
- The algorithm is motivated from zerosum game theory to achieve a robust prediction

Figure 42 Welding system with real time NDE and machine learning.

Features & Attributes: Two algorithms are developed:
(1) Assessing weld quality using AE and welding parameters: Features used for GTAW: Average signal level (ASL), Absolute Energy (Abs-Energy), Heat Input Features used for GMAW: ASL, Abs-Energy, Heat Input, Counts, Amplitude, Frequency Centroid, and Peak Frequency
Steps for the prediction model: (i) TDD and Heat Input merged into single file with the same time steps. Linear interpolation is used to bring the data to the same sampling rate. (ii) Quality labels (e.g., good weld, porosity) are provided for each data set. (iii) The data is trained using Adversarial Sequence

Tagging method. (iv) The model is stored for testing. (v) Model predicts the test samples which are similarly processed as in steps i-ii.

(2) Assessing weld penetration with UT:
The correlation between weld morphology and UT energy ratio is built for GTAW and GMAW. The experimental results are validated by numerical models. Using the regression models, unknown weld morphology can be predicted using the UT energy ratio.

Modes of Operation: This is a real-time and in-situ monitoring approach. The operation is automated through scanner and software. While all the experiments in this project are conducted with automated welding, the AE sensors can be attached to manual or automated welding systems. As the current scanner can move only one directional, single line and groove weld type is studied. A fixture can be designed to attach to welding torch for tracking more complex weld geometries such as tee joints and fillet welds. If the acoustic environment changes, a new training set is required.

Software Development Documentation/Design Document: All the software details are prepared in 'readme' document and shared with UILabs for sharing with DMDII members.

Users & Use Cases: The algorithm is developed using data from two different laboratories. The major user of GMAW results is heavy industry such as Caterpillar and John Deere. An example of use case for automated or manual welding is the following: "As a welding engineer, I want to have the ability to stop the process as soon as possible if the weld quality is not satisfactory such that I can change the input variables and eliminate the ruining of entire expensive welded pieces." The automation of decision making minimizes qualitative visual assessment or the experience of welding engineering who can differentiate the sound of weld depending on its quality. AE sensors and machine learning algorithms digitize the human ear and eliminate any speculative weld assessment.

V. ACCESSING THE TECHNOLOGY

A MEMS device has background IP. Ozevin's group designed MEMS acoustic emission sensors with the transduction mechanism of capacitance change. The sensors were manufactured by MEMSCAP. In this project, we used the same foundry but different manufacturing method. Piezoelectric-based MEMS sensors were designed and manufactured with piezo-MUMPs process. The access to technology is available through the UIC Office of Technology Management.

The required equipment for AE includes sensors, data acquisition system and processor to extract AE features real time. The welding system should be instrumented with current sensor, voltage sensor, gas flow rate sensor and travel speed sensor, and digitized real time. The required equipment for UT includes air-coupled sensors, data acquisition system and processor to extract UT features in-situ. The expertise needed to evaluate the results requires welding background as well as nondestructive evaluation background. However, once the algorithm is automated with high accuracy prediction, the NDE expertise can be omitted.

VI. INDUSTRY IMPACT & POTENTIAL

The market/commercialization analysis prepared by the UIC Office of Technology Management for real-time weld quality assurance is described below.

- Analysis put forth by a MarketandMarkets report expected the robot welding market to grow from as estimated USD 3.89 billion in 2018 to USD 5.96 billion by 2023
- CAGR of 8.91% from 2018 -2023
- Spot welding is expected to be the largest share of the robotic welding market
- Asia-Pacific is expected to be the fastest growing market
- Payload over 150kg are expected to dominate the market

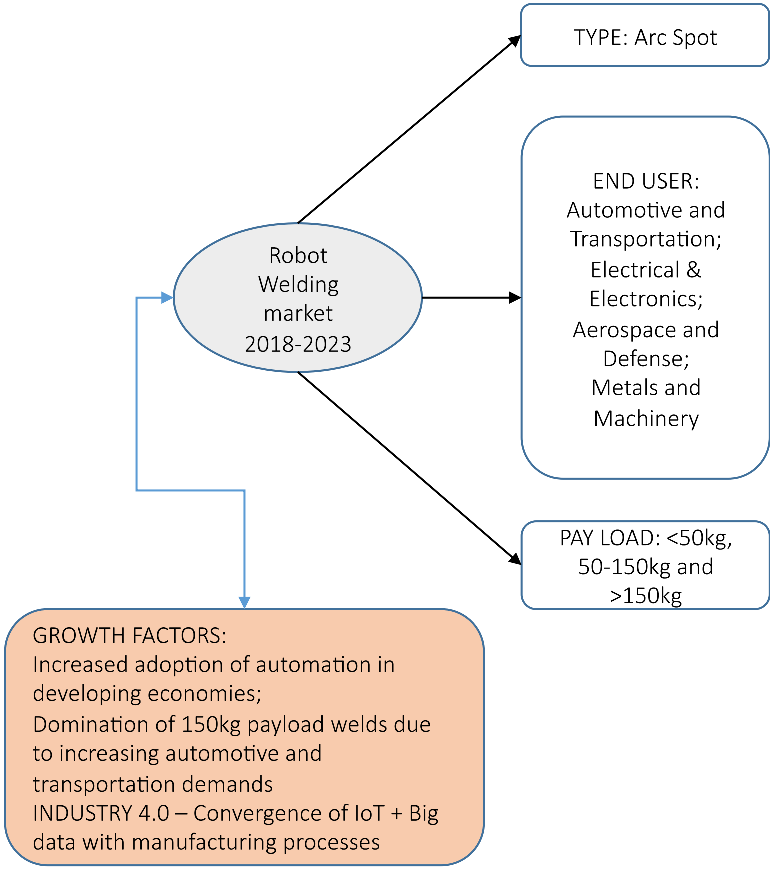

The market/commercialization analysis prepared by the UIC Office of Technology Management for MEMS device is described below.

- The structural health monitoring market is estimated to grow from USD 701.4 million in 2015 to USD 340.7 million by 2022 at a CAGR of 24.99% between 2016 and 2022 (Source – Marketsandmarkets report, 2015).
- Key Target Markets: civil engineering and architectural service providers; sensor manufacturers; aerospace and defense original equipment manufacturers (OEMS); construction firms; system integration; government and research organizations

While the project is aimed for specific welding process, the outcomes are valid for any welding processes such as aerospace, automotive, energy, and shipbuilding. For instance, the complexity of welded geometries diminishes the use of air-coupled UT real-time. This is applicable to heavy industry to automobile industry. The machine learning algorithm and the feature set are also applicable to different weld setting. However, as the weld inputs and the acoustic environment change from one process to another, new training set is needed. The size of training set is controlled by number of variables, level of accuracy and number of defect types. Typically, at least three repetitive data sets representing one condition (thickness, material, defect type etc.) are needed.

VII. TECH TRANSITION PLAN & COMMERCIALIZATION

Currently, machine learning algorithms are developed using intentionally introduced defects into the welded plates. We can move forward to take the technology from laboratory-scale to industrial-scale if we can follow two-step process outlined below.

Step 1 – Discussions on adding acoustics data into ArcAgent hardware and then the trained machine learning algorithm into centerpiece software.

Step 2 – Looking for interested parties (e.g. Caterpillar, John Deere) to test hardware/software in real welding platform to collect more data and validate the algorithm.

During discussions at John Deere, the welding engineer indicated that “As a welding engineer, I want to stop welding if it starts producing a detected weld so that I can fix the parameters and improve the weld quality without wasting the entire piece.” That is the foundation of technology transition plan. In commercialization plan, all hardware/software will be integrated into a single platform to deliver a final product applicable to different arc welding processes.

The requirements for successful technology transfer include (1) participants from different weld manufacturers, (2) instrumentation of at least ten welding equipment for daily data collection, (3) weld equipment manufacturer to add acoustic data and machine learning data together with machine learning algorithm into their controller systems, (4) software platform to integrate all the data for real time assessment. The proposed high level architecture to generate large data sets and develop a deployable machine learning system is shown in Figure 43. Using the data generated and analyzed in this project, the preprocessing steps are defined, and the best performing machine learning algorithm is selected. It is envisioned to deploy ten stations instrumented with welding sensors and acoustic emission sensors such that data from different robotic or manual welds will be collected on a daily basis. The data will be processed using Azure Microsoft Machine Learning Software using the selected algorithm programmed into Azure with Python. The algorithm will use time series modeling for sequential predictions to recognize differences in weld properties based on accumulated evidence over time and be adjustable to balance false positive and false negative rates for burn-through, porosity, and other specified weld categories, as desired by the end user. We will provide variants for both making online prediction (i.e., real-time alerts of defects) and making offline predictions (i.e., retrospective detection of defects). For certain stations, we will produce replica of welded samples without disrupting the manufacturing process in order to improve the training set and validate the testing set results. Other replicas will be produced at UIC laboratory. Those stations will also be instrumented with cameras for visualization.

As discussed above, minimum three repetitive data sets are needed for each specific condition for supervised classification. Another approach is to collect data and understand similarity and differences in unsupervised mode. However, the final assignment of classes requires additional inputs. At the end, number of variables, need of accuracy and number of defects control the required number of data sets for training and testing.

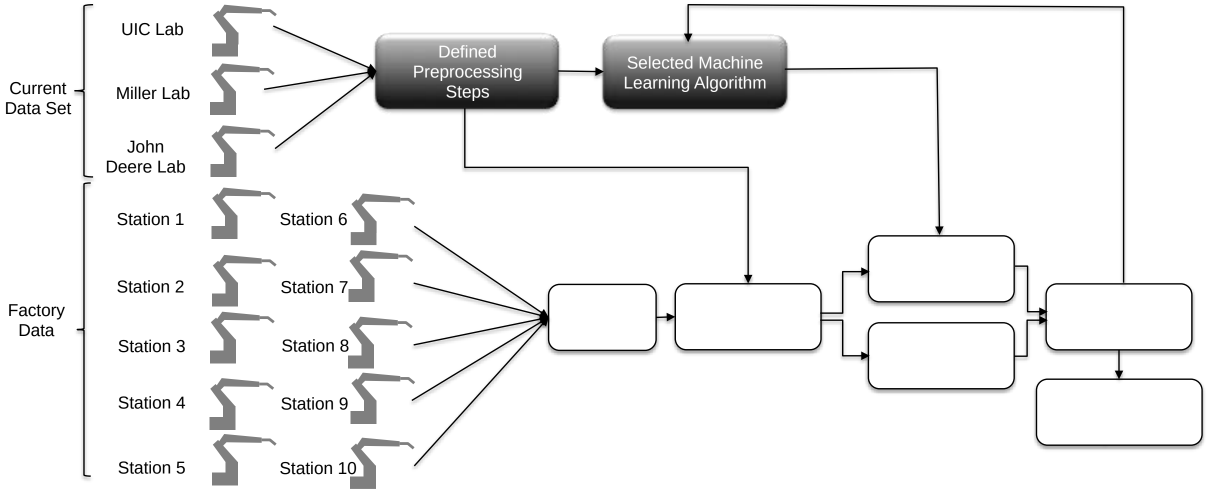

Figure 43 The system architecture to produce big data.

VIII. WORKFORCE DEVELOPMENT

The project involved several M.S. and Ph.D. students. Their names and current positions are described below.

- Dr. Lu Zhang (recently graduated and started as post-doc at UIC): Dr. Zhang gained expertise on numerical modeling of ultrasonics and welding process. He led many journal manuscripts and conference proceedings as a result of this project.
- Alexandra-Del-Carmen Basantes-Defaz (graduated M.S. student and started working as quality control engineer) – Ms Basantes-Defaz improved her background on nondestructive evaluation of welding process. She worked closely with Dr. Zhang and Dr. Ahmad and Mr. Asif for producing data for the machine learning algorithm. Her photograph and essay about welding was placed as the second in highly competitive Image of Research competition at UIC in 2017, see the photograph below.
- Dr. Zeynab Abbasi (currently Senior Engineer at Thornton Tomasetti) – Dr. Abbasi conducted the initial UT experiments, and developed the energy ratio – weld quality relationships.
- Dr. Nasir Ahmad (started as post-doc at Arizona State University) – Dr. Ahmad applied pre-processing steps to identify the most effective features, and wrote the data integration algorithm.
- Kaiser Asif (Ph.D. student) – Mr. Asif is the PhD student leading the machine learning algorithm development together with Professors Ziebart and Derrible. Through this project, he has better understanding of manufacturing process and valid data sets for the algorithms.
- Hanie Kazari (PhD. student) – Ms. Kazari worked with Dr. Kabir on the design, fabrication and characterization of MEMS device. She secured internship at Knowles in summer 2018. She particularly led the characterization of MEMS UT sensors.
- Dr. Minoo Kabir (started as post-doc at Stanford University) – Dr. Kabir led the design, fabrication and characterization of MEMS device. She particularly led the characterization of MEMS AE sensors.
- Dr. Amir Mostavi (started as project engineer at Skanska) – Dr. Mostavi applied nonlinear ultrasonic technique to welding parts for increasing the accuracy to detect heterogeneities.

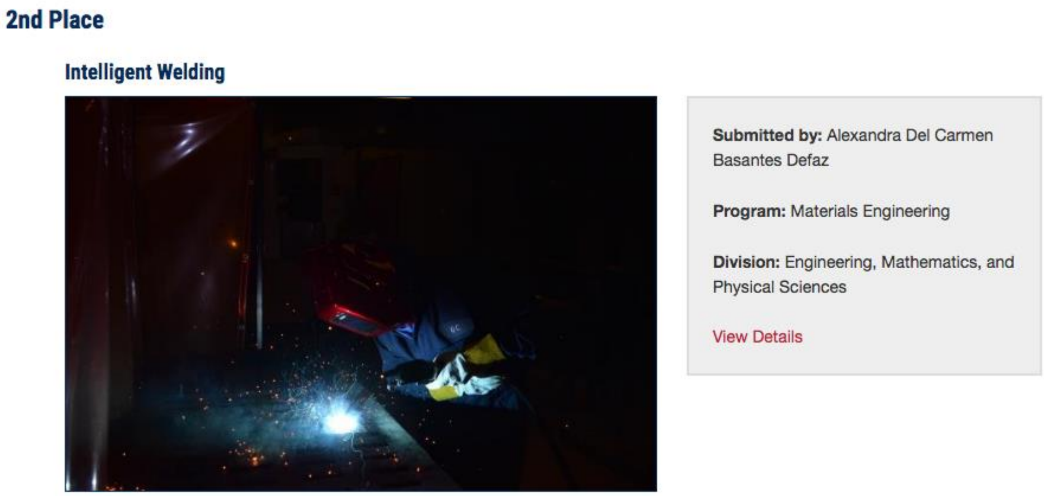

2nd Place

Intelligent Welding

Submitted by: Alexandra Del Carmen Basantes Defaz

Program: Materials Engineering

Division: Engineering, Mathematics, and Physical Sciences

View Details

Figure 44 Image of Research photography by Alexandra-Del-Carmen Basantes-Defaz.

In addition to graduate students participated to the project, the project content was utilized in CME 594 Characterization of Materials by Nondestructive Testing, co-taught by Professors Indacochea and Ozevin. One of the group projects is titled as ‘Study of Burn-through in Welded Steel Samples using Ultrasonic Techniques’ in Fall 2017. The students applied variety of UT methods to correlate with weld penetration experimentally in addition to numerical models. The course is taught every other year, and the results of this project will be included in future sessions. Professor Indacochea teaches Welding course every other even fall semesters. He also utilizes the welding tool and he project outcome. The average number of students in both courses is between 15-20.

IX. CONCLUSIONS/RECOMMENDATIONS

In this project, a real-time assessment method of weld quality was developed. The followings are the major conclusions and recommendations of this study:

Real-time Nondestructive Evaluation Methods for Welding Monitoring: In the original scope of acoustic emission, ultrasonics and thermal methods were selected as non-intrusive NDE methods for monitoring the welding process. It is concluded that ultrasonic testing is not applicable to field conditions due to complex movement of welding torch, and the influence of electromagnetic field. Thermal sensing is influenced by surface emissivity. Therefore, it is determined that acoustic emission is the most appropriate NDE method for real time welding monitoring.

Recommendation: A fixture adaptable to welding torches should be designed to make the NDE method more flexible instead of 1D scanning capacity.

The Selection of Feature Set for Machine Learning Algorithm: GTAW is an acoustically quite process. Therefore, acoustic features obtained from time driven data (absolute energy and ASL) are further manipulated to generate new features and enrich the feature set. The average, the minimum, the maximum, and the accumulation rate values of absolute energy in 200 ms windows are calculated. Accumulation rate is the difference between the linear accumulation and the real accumulation. GMAW is acoustically noisy process. In addition to time driven data utilized for GTAW, hit driven data of count, amplitude, frequency centroid and peak frequency are identified as the most sensitive AE features to the welding state.

Recommendation: The characteristics of other weld defects (e.g., crack) should be identified. However, designing samples with unique defects is a challenge. Therefore, acoustic data from different laboratories should be collected to build the AE data bank for welding. When more data is collected, the acoustic characteristics of defects can uniquely be identified.

Machine Learning Algorithm: For this project, we adopted the Adversarial Sequence Tagging (AST) machine learning algorithm that takes into account the time sequence of the welding as a whole and predicts weld quality at each time point in such a way that minimizes the overall error. As a result, the presence of erroneous or spurious values in the data at some intermediate position of a sequence did not impact the performance of the model. Weld quality was treated as a classification insofar as the goal was to predict the "class" of weld; i.e., *good*, *burn-through*, or *porosity*. Once the synchronized features were loaded, we scaled each feature to be in the range of [0,1]. Then, we performed a quadratic transformation; i.e., each feature is multiplied by every other feature. This represented an interdependent feature relation. We then fed this final feature-set to the model for training and prediction.

Recommendation: The improvement of machine learning accuracy is dependent on data set. More data is needed to increase the resolution and accuracy of machine learning algorithm.

In-situ Assessment of Weld Morphology and Heterogeneity with Ultrasonics: Ultrasonic testing (UT) has advantages over optical and thermal methods in efficiency, cost-effectiveness, and sensitivity to microstructure. UT is an active NDE method that evaluates materials through measuring the change in the properties of propagating waves generated by a transmitter. UT can be categorized as (i) linear UT (LUT) and (ii) nonlinear UT (NLUT). LUT measures wave attenuation, wave velocity or linear resonance frequency to detect defects in materials. The resolution of LUT is limited to the wavelength of ultrasonic signal. On the other hand, NLUT method is able to detect microscopic imperfections in sub-wavelength, employing the nonlinear principles of wave propagation. One of the NLUT methods is called second harmonic generation (SHG). SHG is based on the generation of second harmonic frequency component in materials associated with nonlinear elasticity. Micro-structural heterogeneities can cause nonlinear elasticity such as nucleated voids, precipitate coarsening and dislocation density

In this project, burn-through defects with different penetration levels were introduced by increasing the welding current or reducing the travel speed while keeping the other welding parameters constant. The Lamb-wave-based approach for airborne ultrasonic testing was then applied in order to correlate various ultrasonic features with significant changes in the weld microstructure. For LUT, numerical models were built using the weld morphology obtained experimentally and the weld material properties provided in the literature. The results show that the burn-through defect lead to a larger volume of degraded weld zone, providing a resistance path for the wave to travel, which results in a lower velocity, energy ratio, and amplitude. Additionally, the wave energy disperses due to the increase of burn-through defect, resulting in higher attenuation. Two UT features—energy ratio and frequency—can be used to accept/reject the weld through detection of burn-through damage and identify the welding parameters causing the burn-through damage. If contact sensors are used, it is observed from the results of the LUT using 1 MHz transducers that the UT energy ratio decreases about 46% as the heat input increases from 0 to 1.5 kJ/mm, while the UT energy ratio calculated using 500 kHz transducers does not indicate any correlation with heat input. The linear UT frequency is limited in this study to 1 MHz to reduce the influence of surface roughness and curvature. Using NLUT, it is observed that the relative acoustic nonlinearity parameter (β') is more sensitive to weld morphology than LUT. The value of β' increases by 350% as the heat input increases from 0 to 1.5 kJ/mm. This means that β' is almost 7.6 times more sensitive to the heat input (i.e., weld morphology) than the UT energy ratio.

Recommendation: Bead-on-plate welds are studied in this project. More complex welds should be built to apply LUT and NLUT to detect the weld morphology and heterogeneities as well as residual stress.

Miniaturized Multi-Sensor Device: To address the goal of cost effective weld monitoring, AE and UT sensors were designed, fabricated and characterized using Micro-Electro-Mechanical-Systems (MEMS). The piezo-MEMS AE and UT sensors were developed using piezoMUMPs provided by MEMSCAP, which have advantage over the capacitive type MEMS sensors due to no DC power requirement to operate. The MEMS device contained two AE sensors with the design resonant frequencies of 40 kHz (LF sensor) and 200 kHz (HF sensor). The LF sensor was uniquely designed with a mass of entire silicon substrate in order to reduce the overall size of sensor while tuning it to lower frequency. The MEMS UT array was tuned to 1 MHz and their operations as transmitter and receiver were demonstrated. The sensitivities of piezo-MEMS sensors taking into account their sizes are comparable to conventional piezoelectric sensors.

Recommendation: To increase the sensitivity of the designed piezo-MEMS AE sensors, a group of 25 unit cells can be connected in a 5 × 5 array to reach to the sensitivity of conventional AE sensors. The package requires improvements for reducing electronic noise, and the shielded cables.

In summary, the combination of AE and UT methods provide qualitative and quantitative description of welding process and morphology. With the miniaturization of AE and UT sensors, the sensor cost can be significantly reduced, which opens potentials to instrument many welding systems with AE and UT sensors.

X. LESSONS LEARNED

a. Problems Encountered:

The problems encountered in each development item are summarized below in the same order as the conclusion section.

Real-time Nondestructive Evaluation Methods for Welding Monitoring: UT is negatively affected by electromagnetic field induced by the welding torch. Additionally, airborne UT is sensitive to slight changes in angles between transducer and surface. It is difficult to track welding torch with complex movements. In addition to two air-borne UT sensors as transmitter and receiver, the mix of air-borne UT as receiver and rolling UT as transmitter was studied. While more encouraging results were obtained, the approach is only applicable to 1D welding; on the other hand, the factory level welding, especially robotic welding, has more complex maneuver. It is concluded that UT is not suitable as real time NDE. Thermal sensor also resulted in inconsistent results due to surface emissivity.

The Selection of Feature Set for Machine Learning Algorithm: The project team spent significant effort to prepare the samples at the UIC laboratory using GTAW. At the end, GTAW became to be an acoustically quite process leading to insufficient data for differentiating classes. Therefore, the project team then spent significant time to produce new feature sets. This caused delay to produce sufficient samples for machine learning algorithm. From the lessons learned at the UIC laboratory, the team could collect much richer data set at John Deere laboratory for GMAW, which is acoustically active process leading to strong and process-dependent data sets.

Machine Learning Algorithm: The variables in welding process (manufacturing methods as GMAW or GTAW, plate thickness, materials properties, weld defects) are significant. The manufacturing of sample sets including individual or concurrent variables is required for robust machine learning algorithm.

Miniaturized Multi-Sensor Device: While all the sensors are functional at their design frequencies, the sensitivities, especially AE sensors, should be increased. In the design, one unit cell is used to design AE sensors. It would be ideal to combine at least ten unit cells to increase the sensitivity by ten times. As discussed above, as the machine learning algorithm is data-driven, new data needs to be collected when MEMS sensors are used.

b. Plan/Scope of Work/Proposal Claim Deviations:
In the original proposal, GMAW was proposed to be studied. However, based on the initial discussions with ITW Miller, we switched to GTAW due to better control variables. After conducting many welding with GTAW, the team has limited success with the machine learning algorithm of GTAW due to insufficient data. The welding process was modified to GMAW after discussions with Caterpillar as this is the dominant welding process for heavy industry. Using a controlled experimental plan, a more robust algorithm was developed for GMAW.

In the original proposal, it was proposed to include AE, UT, thermal, and welding data to train the machine learning algorithms. The UT limitations are discussed above. Thermal sensor is also affected by surface emissivity. Therefore, various AE features and welding inputs were utilized in the machine learning algorithms.

MEMS sensors were planned replacing conventional AE and UT sensors. While all the sensors on the MEMS device function properly, they need more robust packaging to survive in harsh welding environment and decrease electronic noise.

c. Risks Realized

The project risks include (1) overlapping feature characteristics for multiple failure modes, (2) not functional MEMS device, (3) insufficient sensitivity of MEMS and (4) insufficient response time. For the first risk, the team developed new feature sets extracted from AE and UT data to reduce the overlapping features, and confusion matrix. For the second and third risks, all the MEMS sensors were functional. However, they could not be tested during welding due to problems faced with packaging and high noise. Conventional sensors were utilized not to delay the data generation for the machine learning algorithm. For the fourth risk, the team determined the computation time of testing set is within seconds. This is sufficient to stop the process and modify the welding parameters.

XI. DEFINITIONS

AE: Acoustic Emission

UT: Ultrasonics Testing

GTAW: Gas Tungsten Arc Welding

GMAW: Gas Metal Arch Welding

NDE: Nondestructive Evaluation

MEMS: Micro-Electro-Mechanical Systems

HDD: Hit Driven Data

TDD: Time Driven Data

ASL: Average Signal Level

LF: Low-Frequency

HF: High-Frequency

DC: Direct Current

XII. APPENDICES

A. List Document Deliverables
B. Validation & Testing
    1. Description of Miller Data
    2. Description of John Deere Data
C. Publications Summary

Appendix A - Document Deliverables

- Digital Real-Time Response Algorithm for GTAW
- Digital Real-Time Response Algorithm for GMAW
- User Manual
- UIC Welding Data
- Miller Welding Data
- John Deere Welding Data
- Final Report
- MEMS Sensor Design

Appendix B. Validation & Testing

Description of Miller Samples

Table 8 The description of weld samples at UIC laboratory.

#	Sample Name	Current(A)	Gas Flow (feet^3/h)	Travel speed (in/min)	Heat Input (kJ/in)	Expected weld defect
1	BT1	160	35	8	11.3	intermediate heat input
2	BT3_1	300	37	6	39.4	burn-through
3	BT3_2	300	37	5.5	36.8	burn-through
4	BT4_1	160	35	4.26	23.8	high heat input
5	BT4_2	160	35	2.14	43.3	burn-through
6	BT6_1	160	35	8	10.9	burn-through
7	BT6_2	160	35	2	41.5	burn-through
8	BT7_1	160	35	6.4	12.2	intermediate heat input
9	BT7_2	160	35	4.26	21.1	intermediate heat input
10	BTV2_1	160	35	8	11.4	good weld
11	BTV2_2	160	35	6.4	13.9	intermediate heat input
12	BTV2_3	160	36	5.12	17.7	intermediate heat input
13	BTV2_4	160	36	4	21.7	high heat Input
14	RTGW2	160	35	8	10.1	good weld
15	RTGW3**	160	35	8	9.2	good weld
16	RTGW4	150	35	8	9.5	good weld
17	RTGW5(GW) **	150	35	8	9.0	good weld
18	RTBT2_2(BTT1)	200	35	8	15.6	intermediate heat input
19	RTBT3_2(BTT2)	230	35	8	18.2	intermediate heat input
20	RTBT3_3	230	35	8	17.5	intermediate heat input
21	RTBT4	150	35	4	18.9	high heat Input
22	RTBT4_3(BTT3)	230	35	6	23.1	high heat Input
23	RTBT4_4	230	35	6	21.7	high heat Input
24	RTBT5_1**	230	35	3	36.1	burn through
25	RTBT7_1	230	35	5	25.7	high heat Input
26	RTBT8**	160	35	2	38.2	burn through
27	ML1*	160	35	8/2.8/5	10.2/25.6/13.4	mix categories
28	ML2*	200	35	4.5/3/11	36.7/8.6/7.8	mix categories
29	ML3*	180	35	5/12/4	19.4/7.2/21.1	mix categories
30	ML4*	220-150	35	3/7.5/6	22.1/8.4/12.4	mix categories
31	ML5*	200	35	7/2.5	12.4/34.6/6.3	mix categories
32	P1	160	30	8	11.4	porosity
33	SP6_1	160	35	8	13.2	porosity
34	SP6_2	160	35	8	11.9	porosity
35	SP7_1	160	35	6.4	12.1	porosity
36	SP7_2	160	35	4.26	19.9	porosity
37	SP8_1	200	35	8	15.6	porosity
38	SP8_2	200	35	8	15.8	porosity
39	BTm1	100	20	8	6.2	porosity

* Test data set **Train data set

Description of Miller Samples

Table 9 The description of weld samples at Miller laboratory.

GMAW Process

ThicknessPlate	**Joint Details**	**Sample**		**Welding**	**Amp.**	**Voltage**	**Gas Flow**	**Travel Speed**	**Heat Input**	Expected weld defect
mm		each		passes	A	V	m3/h	mm/min	kJ/mm	
3/16in (4.76mm) plate	Bead on plate	S1	W1	Single pass	254.40	26.73	0.96	400	1.02	Excessive penetration
	Bead on plate	S2	W1	Single pass	260.00	29.00	0.96	650	0.70	Good weld
			W2	Single pass	261.00	26.18	0.99	750	0.55	Good weld
	Bead on plate	S3	W1	Single pass	258.00	26.42	0.97	550	0.74	Penetration
			W2	Single pass	268.08	27.40	0.96	450	0.98	Excessive penetration
	Square groove weld (PJP)	S4	W1	Single pass	246.65	25.75	0.95	650	0.59	Square Groove
			W2	Single pass	274.74	28.04	0.96	750	0.62	Square Groove
	Bead on plate	S5	W1	Single pass	264.17	27.14	0.95	850	0.51	Good weld
			W2	Single pass	261.06	27.44	0.99	700	0.61	Good weld
1/2in (12.70 mm) plate	Single V groove weld (PJP)	S6	W1	Root pass	265.08	26.99	0.95	850	0.51	V groove
				Filler pass	263.62	26.66	0.96	250	1.69	V groove
			W2	Root pass	264.41	27.64	0.95	500	0.88	V groove
				Filler pass	253.79	26.68	0.95	300	1.35	V groove
	Single V groove weld (PJP)	S7	W1	Root pass	262.40	26.24	1.05	400	1.03	V groove
				Filler pass	263.44	26.73	1.03	300	1.41	V groove
			W2	Root pass	267.35	26.07	1.03	300	1.39	V groove
				Filler pass	257.39	26.56	1.03	250	1.64	V groove

GTAW

Thickness Plate	**Joint Details**	**Sample**		**Welding**	**Amp.**	**Voltage**	**Gas Flow**	**Travel Speed**	**Heat Input**	Expected weld defect
mm		each		passes	A	V	m3/h	mm/min	kJ/mm	
3/16in (4.76mm) plate	Bead on plate	S8	W1	Single pass	156.00	10.43	0.47	203.20	0.48	good weld
					195.00	10.45	0.47	203.20	0.60	good weld
					245.00	10.47	0.47	203.20	0.76	good weld
	Bead on plate	S9	W1	Single pass	156.00	10.43	0.47	203.20	0.48	good weld
					195.00	10.45	0.47	203.20	0.60	good weld
					245.00	10.47	0.47	203.20	0.76	good weld
	Bead on plate	S10	W1	Single pass	293.50	12.41	0.47	203.20	1.08	Excessive penetration
			W2	Single pass	293.50	12.45	0.47	152.40	1.44	Burn-through (with hole)
			W3	Single pass	293.34	12.45	0.49	177.80	1.23	Burn-through (with hole)
	Bead on	S1	W1	Single pass	160.00	10.00	0.48	162.56	0.59	good weld

	plate	1	W2	Single pass	160.00	10.50	0.49	130.05	0.78	Penetration
			W3	Single pass	160.00	10.50	0.49	101.60	0.99	Penetration
	Bead on plate	S12	W1	Single pass	157.00	10.50	0.48	108.20	0.91	Penetration
			W2	Single pass	156.00	10.50	0.48	54.36	1.81	Excessive penetration
	Square groove weld (PJP)	S13	W1	Single pass	176.40	10.50	0.48	203.20	0.55	Square groove
					156.62	10.00	0.48	203.20	0.46	Square groove
					137.50	10.00	0.48	203.20	0.41	Square groove

GTAW - Creating porosity

Thickness Plate	**Joint Details**	**Sample**		**Welding**	**Amp.**	**Voltage**	**Gas Flow**	**Travel Speed**	**Heat Input**	Expected weld defect
mm		each		passes	A	V	m3/h	mm/min	kJ/mm	
3/16in (4.76mm) plate	Bead on plate	S14	W1	Single pass	157.00	10.50	0.57	203.20	0.49	porosity
			W2	Single pass	157.00	10.50	0.57	203.20	0.49	porosity
			W3	Single pass	157.00	10.50	0.57	203.20	0.49	porosity

Description of John Deere Samples

Table 10 The description of weld samples at John Deere.

#	Sample Name	Wire speed (in/min)	Gas Flow (feet^3/h)	Travel speed (mm/s)	Heat Input (kJ/mm)	Expected weld defect
1	JD-P1-TS-1**	200	40	11	0.38	Good weld
2	JD-P1-TS-2*	200	40	11	0.38	Good weld
3	JD-P1-TS-3*	200	40	11	0.38	Good weld
4	JD-P2-TS-1*	160	40	11	0.3	Good weld
5	JD-P2-TS-2*	160	40	11	0.3	Good weld
6	JD-P2-TS-3*	160	40	11	0.3	Good weld
7	JD-P3-TS-1*	120	40	11	0.2	Good weld
8	JD-P3-TS-2*	120	40	11	0.2	Good weld
9	JD-P3-TS-3*	120	40	11	0.2	Good weld
10	JD-P4-TS-1**	100	40	11	0.18	Good weld
11	JD-P4-TS-2*	100	40	11	0.18	Good weld
12	JD-P4-TS-3*	100	40	11	0.18	Good weld
13	JD-P5-TS-1**	240	40	11	0.49	Penetration
14	JD-P5-TS-2*	240	40	11	0.49	Penetration
15	JD-P5-TS-3*	240	40	11	0.49	Penetration
16	JD-P6-TS-1**	260	40	11	0.52	Penetration
17	JD-P6-TS-2*	260	40	11	0.52	Penetration
18	JD-P6-TS-3*	260	40	11	0.52	Penetration
19	JD-P7-TS-1*	280	40	11	0.58	onset of burn-though
20	JD-P7-TS-2*	280	40	11	0.58	onset of burn-though
21	JD-P7-TS-3*	280	40	11	0.58	onset of burn-though
22	JD-P8-TS-1**	300	40	11	0.6	burn-though (w hole)
23	JD-P8-TS-2**	300	40	11	0.6	burn-though (w hole)
24	JD-P8-TS-3*	300	40	11	0.6	burn-though (w hole)
25	JD-P1-PO1-1*	200	25	11	0.39	Good weld
26	JD-P1-PO1-2*	200	25	11	0.39	Good weld
27	JD-P1-PO1-3*	200	25	11	0.39	Good weld
28	JD-P1-PO2-1*	200	21	11	0.4	Good weld
29	JD-P1-PO2-2*	200	21	11	0.4	Good weld
30	JD-P1-PO2-3*	200	21	11	0.4	Good weld
31	JD-P1-PO3-1**	200	12	11	0.39	porosity
32	JD-P1-PO3-2**	200	12	11	0.39	porosity
33	JD-P1-PO3-3*	200	12	11	0.39	porosity
34	JD-P1-PO3-4*	200	12	11	0.39	porosity
35	JD-P1-PO3-5*	200	12	11	0.39	porosity
36	JD-P7-PO3-1*	280	12	11	0.56	Penetration +porosity
37	JD-P7-PO3-2*	280	12	11	0.56	Penetration +porosity
38	JD-P7-PO3-3*	280	12	11	0.56	Penetration +porosity
39	JD-P7-PO3-4*	280	12	11	0.56	Penetration +porosity
40	JD-P7-PO3-5*	280	12	11	0.56	Penetration +porosity
41	JD-P7-PO4*	280	56	11	0.56	Penetration +porosity
42	JD-P7-PO5*	280	59	11	0.56	Penetration +porosity

* Test data set   **Train data set

Appendix C. Publications Summary

Journal Manuscripts

Zhang, L. Mostavi, A., Basantes-Defaz, A.C., Ozevin, D. and Indacochea, E., "The Measurement of Weld Morhology and Inclusions using Ultrasonics, Measurement, *doi.org/10.1016/j.measurement.2019.04.088*, 2019.

Zhang, L., Basantes-Defaz, A.C., Ozevin, D. and Indacochea, E. "Real-time Monitoring of Welding Process using Air-coupled Ultrasonics and Acoustic Emission," International Journal of Advanced Manufacturing Technologies, doi.org/10.1007/s00170-018-3042-2, 2018.

Kabir, M., Kazari, H. and Ozevin, D. "Piezoelectric MEMS Acoustic Emission Sensors," Sensors and Actuators A: Physical, https://doi.org/doi:10.1016/j.sna.2018.05.044, 2018.

Abbasi, Z., Yuhas, D., Zhang, L. Basantes, A.D.C., Tehrani, N.N., Ozevin, D. and Indacochea, E. "The Detection of Burn-through Weld Defects using Noncontact Ultrasonics," Materials, 11, 128, 2018.

Conference Proceedings

Zhang, L., Basantes-Defaz, A.D.C., Abbasi, Z., Yuhas, D., Ozevin, D. and Indacochea, E. "Real-time Nondestructive Monitoring of the Gas Tungsten Arc Welding (GTAW) Process by Combined Airborne Acoustic Emission and Non-Contact Ultrasonics," SPIE NDE/Smart Structures, Denver CO, March 2018.

Kabir, M., Kazari, H. and Ozevin, D. "Piezoelectric Micromachined Acoustic Emission Sensors for Early Stage Damage Detection in Structures," SPIE NDE/Smart Structures, Denver CO, March 2018.